Synthesis and Characterization of Sputter Deposited YZn Thin Films

by

Riju Philip James Akkarakaduppil

A Thesis Presented in Partial Fulfillment
of the Requirements for the Degree
Master of Science

Approved April 2023 by the
Graduate Supervisory Committee:

Jagannathan Rajagopalan, Co-Chair
Pedro Peralta, Co-Chair
Kiran Solanki

ARIZONA STATE UNIVERSITY

May 2023

ABSTRACT

This thesis presents a study of the microstructure and mechanical properties of Yttrium-Zinc (YZn) thin films. Rare-earth intermetallic compounds have gained significant attention in recent years due to their unique structural and mechanical properties, making them suitable for various applications. However, studies on the Y-Zn system are scarce and there are very few published reports on YZn thin films. The main objective of this study is to investigate the microstructure and mechanical properties of YZn thin films using various experimental techniques.

In this study, YZn films of various thicknesses were synthesized via magnetron co-sputtering: 200 nm, 500 nm, 1 µm, 2 µm and 11.5 µm. Then these samples were annealed at 250°C, 300°C, 350°C and 400°C to investigate their microstructural evolution and mechanical properties. X-ray diffraction (XRD) and scanning electron microscopy (SEM) based techniques have been used to analyze the microstructure and chemical composition of these compounds. The mechanical properties such as hardness and elastic modulus have been measured using nanoindentation.

The results show that the microstructure of YZn thin films is dependent on the annealing conditions. The microstructure of samples deposited at room temperature and those annealed at 250°C and 300°C were found to be amorphous except for the 200 nm YZn film. Annealing at higher temperatures leads to crystallization of the films. Moreover, the results demonstrate that YZn intermetallic thin films have high hardness, which varies with the film thickness and annealing treatment.

This work represents an initial effort to understand the microstructural evolution and mechanical properties of YZn thin films as a function of film thickness and annealing temperatures. The results of this study can be used to guide the design and development of YZn thin films with tailored microstructures and mechanical properties for various applications.

ACKNOWLEDGMENTS

I am grateful to my co-advisors, Prof. Jagannathan Rajagopalan and Prof. Pedro Peralta, whose guidance has played an instrumental role in shaping both my professional and personal growth. Their timely advice has not only helped mold me into a better researcher but also aided in my personal growth, preparing me to face any challenges I may encounter outside of academia. I would also thank my committee member, Prof. Kiran Solanki, for his input and for evaluating my thesis.

I would like to extend my heartfelt appreciation to all those who have supported my personal and professional development during my time at ASU. My professors, who generously shared their knowledge with me throughout my graduate studies without any restraint deserve more than my mere words of appreciation. To my lab mates, Gabe King, Sumeyye Caner, and Amirhossein Shafieizad, I express my gratitude for their support and assistance throughout the past year. I thank Antriksh Sharma for his help with the nanoindentation studies. I would also like to acknowledge the research facilities and staff support I received from the Eyring Materials Center, Arizona. The funding for this research was provided by National Science Foundation grant 2223317 (Metals and Metallic Nanostructures program) and the Los Alamos National lab (Subcontract #635305).

Lastly, I would like to express my profound gratitude to my family and friends whose unwavering encouragement and support made this journey both pleasant and enriching. Their kind words helped me keep up good spirits and led me to the timely completion of this thesis.

TABLE OF CONTENTS

Page

LIST OF TABLES

Table Page

LIST OF FIGURES

Figure Page

Figure Page

CHAPTER 1

INTRODUCTION

The most important materials in the history of material science were discovered serendipitously. Of the many reasons that contribute to this, the nature of the metallic bonding and type of chemical formation reaction are the prime ones that obscure the prediction of crystal structures as well as its relationship with the physical properties of compounds.[1] Intermetallic compounds can be defined as a solid phase of two or more metallic elements with an ordered crystal structure. The crystal structure as well as physical properties of the intermetallic compounds vary considerably from that of their constituents. Most of the known intermetallic compounds are found to fall within a collection of specific families of structural prototypes (examples include the B2, L12, Sigma, Laves-, Heusler-, Hume-Rothery phases). While metal alloys can generally be strengthened by the formation of intermetallic precipitates, alloys composed entirely of intermetallic compounds are stronger. However, intermetallic compounds are generally brittle. Aluminides are usually considered for high temperature applications due to their low density and potential to form a protective oxide coating.[2] Yet another element capable of displaying similar property is Yttrium, which forms passivating thin scales of Yttria (Y_2O_3). Yttrium is typically found in rare-earth minerals such as gadolinite and is thus considered a rare-earth element. Due to its attractive physical and thermal properties, yttrium is often used to enhance the properties of other materials.[3]

B2 intermetallic compounds, which have an ordered BCC structure where the body center is occupied by one type of atom and the body corners by other atoms, have been observed either as a major or as a minor phase in many high entropy alloys. This structure is prominently seen in almost all the cases of alloys containing 3d transition elements.[4] While some of the B2 intermetallic are line compounds, alloys based on NiAl have a much wider range of stoichiometry for forming a B2 structure. NiAl based alloys, as compared to nickel based super alloys, have improved oxidation resistance (due to higher aluminum content), higher melting temperatures and better creep resistance.[2]

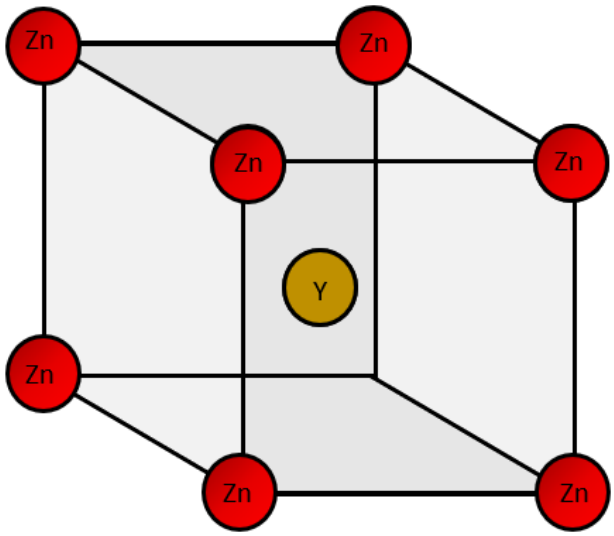

Figure 1: Crystal Structure of B2 YZn.

In the Yttrium-Zinc (Y-Zn) system, a B2 intermetallic compound is formed at the equiatomic composition.[5] Interestingly, no other intermetallic phases are formed at Zn compositions below 50%. While many other B2 intermetallic such as NiAl have been studied in depth, there have been few reports on the microstructure and mechanical

properties of YZn, especially in the thin film form. Therefore, we aim to conduct a characterization of YZn films with varying thickness and different annealing treatments and assess their microstructural and mechanical properties. These investigations can point towards potential applications and expand the knowledge base of B2 forming intermetallics.

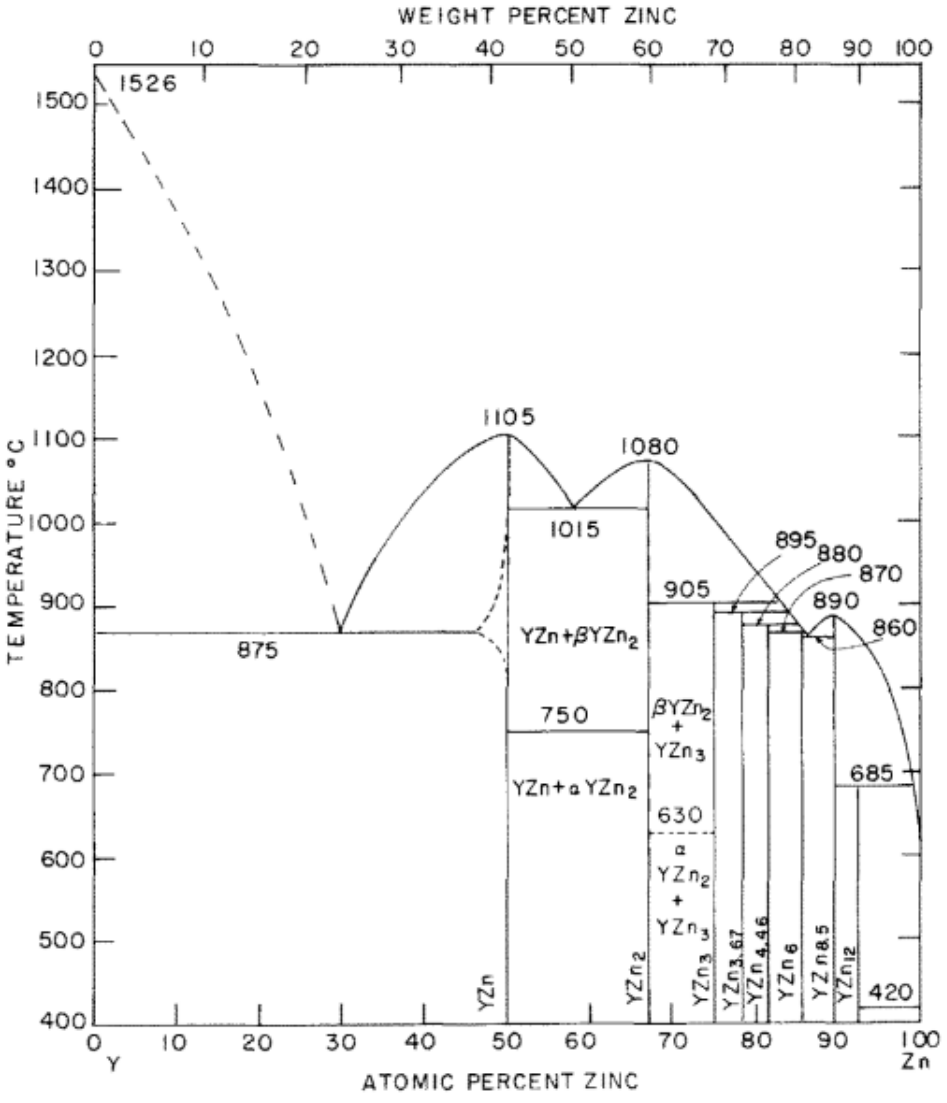

Figure 2: YZn Phase Diagram.[6]

CHAPTER 2

EXPERIMENTAL TOOLS AND METHODS

2.1 Magnetron Sputtering System:

Magnetron sputtering is a versatile thin film deposition technique that can be used to deposit a wide range of materials, including metals, semiconductors, and oxides.[7][8][9] The technique involves the use of a plasma generated by a magnetron, which is used to sputter atoms or ions from a target material onto a substrate. It is a popular physical vapor deposition (PVD) technique used in many research and industrial applications.

A magnetron sputtering system typically consists of a vacuum chamber, a target material, a substrate holder, and a magnetron. The vacuum chamber is used to create a low-pressure environment to facilitate sputtering, and the target material is typically made of the material to be deposited onto the substrate. The substrate holder is used to hold the substrate in place during the deposition process, and the magnetron is used to generate plasma. In this study, an Orion-5 magnetron sputtering system from AJA International was used to perform the depositions of YZn thin films.[10]

Plasma is generated by applying a high voltage to the magnetron, which is typically a circular or rectangular electrode. The high voltage creates an electric field that ionizes the gas in the chamber, generating plasma. The plasma interacts with the target material, sputtering atoms, or ions from the surface of the target onto the substrate. The amount of material deposited onto the substrate can be controlled by adjusting the deposition parameters, such as the power, pressure, and target-to-substrate distance.[10]

The deposition rate (the rate of increase in thickness deposited or in other words the thickness deposited per unit time), can be calculated using the following formula:

$$Number\ of\ atoms\ (N) = {Mass}/{Atomic\ mass}$$

But,

$$Mass = Volume \times Density = Area \times Thickness \times Density$$

So therefore, the equation for number of atoms reduces to,

$$N = \frac{V \times \rho}{m} = \frac{A \times t \times \rho}{m} \qquad \longrightarrow (1)$$

And,

$$\text{Deposition Rate} = {Thickness\ deposited}/{time} = {t}/{T}$$

$$\text{Sputtering Rate} = {Number\ of\ atoms\ sputtered}/{time} = {N}/{T}$$

Using these relations, equation 1 can be rewritten as follows:

$$\text{Deposition Rate} = {(\text{Sputtering Rate} \times \text{Atomic Weight})}/{(\text{Target Area} \times \text{Density})}$$

where the target area is the surface area of the target material, the sputtering rate is the rate at which atoms or ions are sputtered from the target material (atoms or ions sputtered off the target per unit time), the density is the density of the target material, and the atomic weight is the atomic weight of the target material. This formula depicts an ideal case and

the sputter yield, actual ions sputtered and reaching the substrate, might be lower and is impacted by different factors. As such the sputter rate should be replaced with sputter yield for a more realistic picture.

$$\text{Deposition Rate} = {(\text{Sputtering yield} \times \text{Atomic Weight})}\Big/{(\text{Target Area} \times \text{Density})}$$

The AJA Orion-5 magnetron sputtering system uses several advanced features to optimize the deposition process and improve the quality of the deposited films. For example, the system incorporates a rotating substrate holder, which ensures uniform deposition across the substrate. The system also includes advanced plasma monitoring systems and a confocal arrangement of target guns which allows for better control over film properties such as composition, thickness, and morphology.[11] In addition to these advanced features, the AJA Orion-5 sputtering system also incorporates a quartz crystal thickness monitor to calibrate the deposition rates of individual targets as a function of sputtering power. This is crucial to calibrate the deposition rates of Y and Zn and choose appropriate sputtering powers to produce nearly equiatomic YZn films.

Figure 3: AJA Orion-5 Magnetron Sputtering System.[12]

Further for our study here, it is also important to note that the sputtering chamber is capable of annealing and is equipped with a variety of features that enable precise control of annealing parameters, including temperature, gas flow, and vacuum pressure. The temperature of the sample is accurately controlled using a PID controller, which maintains a stable temperature within the chamber during the annealing process. The chamber is also equipped with gas flow control valves that allow for the introduction of different gases,

such as oxygen or nitrogen, during the annealing process. This can be used to modify the chemical composition of the film or to promote the formation of specific crystalline phases.

2.2 Nanoindentation:

Nanoindentation is a widely adopted technique for measuring the mechanical properties of materials at the nanoscale and has become a major technique for determining the mechanical properties of thin films especially.[13] It involves the use of a sharp tip to indent the surface of a material, and the resulting deformation is used to calculate a range of mechanical properties, such as hardness, modulus, and toughness. In this section, we discuss the working of nanoindentation, its applications, and its limitations.

1. Principle of Nanoindentation:

The basic principle of nanoindentation is to apply a small load to the surface of a material using a sharp tip, and then to measure the resulting deformation. The depth of the indentation is typically in the range of a few nanometers to several micrometers, depending on the material and the applied load. The load and displacement data are used to calculate various mechanical properties, such as hardness and modulus. Nanoindentation can be performed using a variety of instruments, including atomic force microscopes (AFMs), scanning electron microscopes (SEMs), and specialized nano indenters.[14] The tip used for nanoindentation can be made of various materials, including diamond, silicon, and tungsten carbide. The tip shape can also vary, with pyramidal and spherical tips being commonly used. In a nano-indentation experiment, the load and displacement data are used to

determine the mechanical properties of the sample, such as hardness and modulus of elasticity. The hardness of a material is defined as the resistance of the material to plastic deformation, while the modulus of elasticity is the ratio of stress to strain in the elastic deformation region. The hardness of the material can be determined by measuring the maximum load applied during the indentation test and dividing it by the area of the indentation:

$$H = {}^{P_{max}}/_{A}$$

where H is the hardness, P_{max} is the maximum load, and A is the contact area between the indenter and the sample surface.[13]

The indentation depth is also measured during the test and can be used to calculate the elastic modulus of the material. The modulus of elasticity is determined by analyzing the elastic deformation region of the load-displacement curve. In this region, the slope of the load-displacement curve is proportional to the stiffness of the sample, which is related to the modulus of elasticity by the following equations:

$$2 \times E_r \times \frac{\sqrt{A}}{\sqrt{\pi}} = \frac{dP}{dz}$$

$$\frac{1}{E_r} = \frac{(1-\nu^2)}{E} + \frac{(1-\nu_i^2)}{E_i}$$

where E and ν are the modulus of elasticity and the Poisson's ratio of the specimen, E_i and ν_i are the same parameters for the indenter. dP/dz is the slope of the unloading curve, E_r is the reduced modulus of elasticity and A is the projected area of elastic contact.[14]

Nanoindentation is a widely used technique to measure the mechanical properties of materials, especially in the field of nanotechnology. However, several variables, such as the size and shape of the indenter, the surface roughness of the sample, and the temperature and humidity of the testing environment can affect the measurements. Therefore, proper precautions should be taken to ensure accurate results.

2. Applications of Nanoindentation:

Nanoindentation has a wide range of applications in materials science and engineering. One of the most common applications is in the characterization of thin films and coatings.[15] Nanoindentation can be used to determine the mechanical properties of these materials, which is critical for understanding their performance in various applications, such as microelectronics and wear-resistant coatings.[16] Another application of nanoindentation is in the study of the mechanical properties of individual nanoparticles.[17] This is important for understanding how the properties of nanoparticles differ from those of bulk materials, and for designing nanoparticles with specific mechanical properties for various applications, such as drug delivery and catalysis. Nanoindentation can also be used to study the mechanical properties of biological materials, such as cells and tissues.[18] This is important for understanding the mechanical behavior of these materials in various physiological processes, such as tissue growth and wound healing.

3. Limitations of Nanoindentation:

While nanoindentation is a powerful technique for measuring the mechanical properties of materials at the nanoscale, it has several limitations that should be considered.

One limitation is that the measured properties are highly dependent on the size and shape of the tip used for indentation.[19] This can lead to errors in the measured values.

The presence of a substrate can result in pileup or sink-in around the indentation, which can affect the measured hardness and modulus values. Furthermore, the substrate can also influence the shape of the indentation, which can make it difficult to extract accurate mechanical properties. Therefore, it is essential to consider substrate effects when performing nanoindentation experiments and to carefully choose the substrate and testing conditions to minimize their impact.[20]

Another limitation of nanoindentation is that the measured properties are highly relative to bulk measurements with potentially artificial trends in modulus as a function of penetration depth.[21]

Finally, nanoindentation can be a time-consuming process, particularly for materials with a low modulus or high toughness. This is because the depth of the indentation is limited by the strength of the material, and a high load may be required to achieve a measurable deformation.

2.3 Powder X-Ray Diffraction:

Powder X-ray diffraction (PXRD) is a widely used analytical technique that is used to determine the structure of crystalline materials. It works by measuring the diffraction of X-rays by a powdered sample, which provides information on the crystal structure, size, and orientation of the crystals. The PANalytical Xpert Pro XRD tool was used to perform the PXRD scans on all the samples.

Figure 4: PANalytical Xpert Pro XRD Machine.[22]

1. X-ray Generation and Delivery:

The first step in PXRD is the generation of X-rays. X-rays are produced by accelerating electrons to high speeds and then colliding with a target material. The choice of X-ray source in PXRD can also affect the scattering process. The most used source is a copper

K-alpha radiation source, which has a wavelength of 1.5406 Å. Other sources, such as synchrotron radiation, can provide higher intensity and more tunable wavelengths, but also require more specialized instrumentation.

2. Sample Preparation & X-ray Scattering:

In PXRD, the sample is usually in the form of a powder, which is spread onto a flat surface. The powder is then gently compressed to ensure that it is evenly distributed and has good contact with the surface. The sample is then placed in the path of the X-ray beam. However, the sample may also be a thin film that is deposited on a substrate.

Since the X-ray scattering process usually involves the interaction of X-rays with a powdered sample containing numerous crystalline grains oriented in different directions, they get scattered in all directions, including in the direction of the detector. The intensity of the scattered X-rays at different angles provides information about the crystal structure, orientation, and composition of the material. The detector used in PXRD must be capable of detecting the weak diffracted X-rays from the sample. Commonly used detectors include scintillation detectors and proportional counters. The choice of detector will depend on factors such as the intensity of the X-ray source and the nature of the sample.

3. Data Analysis:

The diffraction pattern obtained from PXRD provides information about the crystal structure, size, and orientation of the crystals in the sample. The position and intensity of the diffraction peaks can be used to determine the lattice spacing, crystal symmetry, and

crystallographic orientation of the material. By analyzing the diffraction pattern, it is also possible to determine the particle size and degree of crystallinity of the sample.

PXRD allows for the identification of unknown materials, the determination of the crystalline phases present in a sample, and the measurement of the degree of crystallinity of a sample. It is also a non-destructive technique, which means that the same sample can be analyzed multiple times without affecting its properties. PXRD can be used to analyze epitaxial and highly textured thin films as well as films with a random texture. However, the diffracted signal from the underlying substrate can be quite large, making it more difficult to distinguish the peaks corresponding to the thin film and the substrate. Additionally, the diffracted signal from the thin film can be quite weak at very small thicknesses (< 100 nm) due to the limited interaction volume.

2.4 Profilometry:

Profilometry is an analytical technique that is used to measure the surface characteristics of a sample. It provides information on the surface topography, roughness, and texture, which is important in many fields, including materials science, nanotechnology, and manufacturing. There are different types of profilometry techniques in use.

1. Optical Profilometry:

Optical profilometry is the most common type of profilometry. It works by shining a beam of light onto the surface of a sample and measuring the height of the reflected beam. The reflected light is then analyzed to determine the surface characteristics of the sample. The technique is non-destructive and can be used on a wide range of materials, including metals, polymers, and ceramics.

2. Scanning Probe Microscopy:

Another type of profilometry is scanning probe microscopy (SPM), which works by scanning a probe across the surface of a sample. The probe measures the height of the surface as it is scanned, providing information on the topography of the sample. SPM can be used to measure features as small as a few nanometers and is therefore ideal for the study of nanomaterials.

3. Contact Profilometry:

Contact profilometry involves physically contacting the surface of a sample with a probe and measuring the force required to make contact. The force measurement is then used to calculate the height of the surface. The technique is particularly useful for measuring the roughness of a surface, as it can detect even small deviations from a flat surface.

A Dektak profilometer was used for this research. It uses contact profilometry to measure film thickness. The measurements were performed across 4 different patches of undeposited substrate through the YZn film surface. A surface force of 3 mg was found to be ideal so that the stylus doesn't scratch the film surface or cause any deformation. The thickness measurements were found to be around 1% off from the expected thickness values, which happens to be well within the rated error of this device. A sample reading and the figure showing the measurement process can be found in Figure 5 and Figure 6.

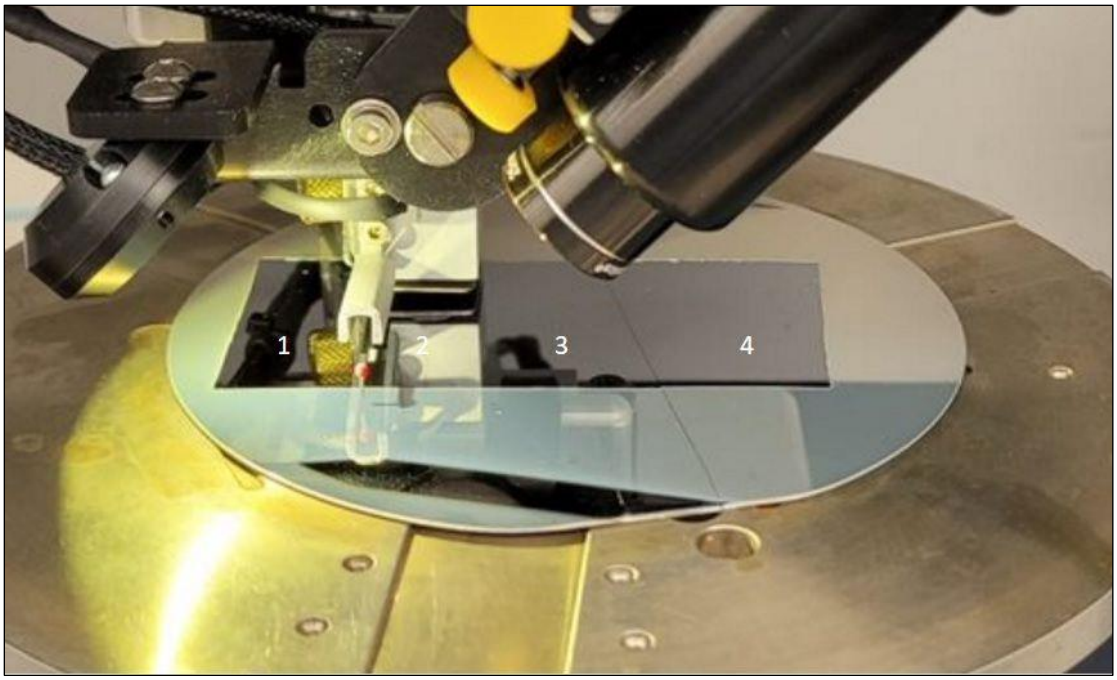

Figure 5: Image Showing the Profilometry Measurements Conducted on 11.5 µm Film.

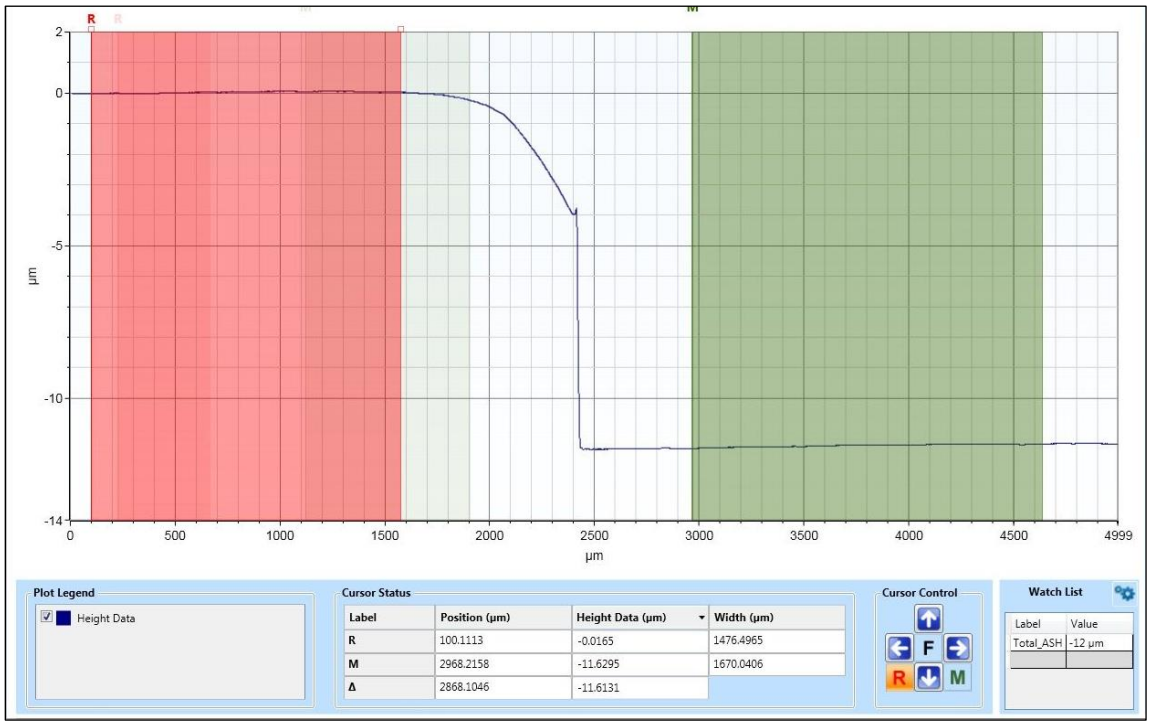

Figure 6: A Typical Profilometry Measurement Result Conducted over 11.5 µm Film.

2.5 Grain size measurement:

The Scherrer equation is commonly used to estimate the average crystallite size or grain size of a thin film from powder X-ray diffraction (PXRD) data:

$$D = \frac{k \cdot \lambda}{\beta \cdot \cos\theta}$$

where D is the average crystallite size, k is a constant usually taken to be around 0.9, λ is the wavelength of the X-ray radiation used, β is the full width at half-maximum (FWHM) of the diffraction peak, and θ is the diffraction angle.[23]

Assumptions:

1) The sample is homogeneous and consists of randomly oriented, uniformly sized, and shaped crystallites or grains.
2) The diffraction peaks are broadened only due to the size of the crystallites or grains.
3) The crystallites or grains are non-strained or have a negligible amount of strain.

Exceptions:

1) The Scherrer equation may yield inaccurate values if the sample contains multiple phases, as the broadening of diffraction peaks may be influenced by factors other than grain size, such as preferred orientation, lattice strain, or solid solution effects.
2) The crystallites or grains in the sample are not spherical in shape, leading to an overestimation of the size. In such cases, more sophisticated analysis techniques

such as the Warren-Averbach method may be used to obtain a more accurate estimate of the grain size.[24]

3) The X-ray peak may be significantly broadened by instrumental factors such as sample displacement, micro-strain in the sample holder, or peak overlap, leading to inaccurate grain size estimation.

CHAPTER 3

SYNTHESIS OF YZn THIN FILMS

3.1 Introduction:

The development of thin film technology has opened a wide range of possibilities for various applications, including electronics, optics, energy harvesting, and sensing.[25] As discussed in Chapter 1, there has been very few reported studies on YZn films, which could have potential applications as a coating material due to its ability to form a passivating oxide layer. To harness the potential of YZn thin films, an efficient and reliable synthesis method is required.

Magnetron sputtering is a well-established technique for the deposition of thin films and multilayers with excellent control over their microstructure.[26][27] Because Y and Zn have very dissimilar melting points and sputtering rates, it is difficult to use a YZn target to synthesize these films while maintaining the correct stoichiometry. However, by co-sputtering Y and Zn this problem can be circumvented since the power applied to the Y and Zn targets can be individually controlled. Hence, in this study we employed co-sputtering from individual Y and Zn sputtering targets to synthesize the YZn thin films.

In this chapter, we will discuss the synthesis of YZn thin films using the AJA Orion-5 magnetron sputtering tool. We will describe the experimental setup and process, and the characterization techniques used to evaluate the properties of the resulting thin films. First, we describe the requirements that need to be satisfied to produce equiatomic YZn films, which is essential to produce the B2 phase.

To produce a YZn film with 50 atomic percent Y and 50 atomic percent Zn, we need to sputter Y and Zn at the appropriate rates so that there are equal number of Y and Zn atoms in the resultant film. Starting with this premise, we need to find the relative deposition rates (thickness per unit time) of Y and Zn that will lead to an equiatomic film,

$$N_Y = N_{Zn}$$

Recalling equation 1 from Section 2.1 of Chapter 2,

$$\frac{V_Y \times \rho_Y}{m_Y} = \frac{V_{Zn} \times \rho_{Zn}}{m_{Zn}}$$

$$\frac{A_Y \times t_Y \times \rho_Y}{m_Y} = \frac{A_{Zn} \times t_{Zn} \times \rho_{Zn}}{m_{Zn}}$$

Since area of deposition (substrate area) is same for both Y and Zn,

$$\frac{t_Y}{t_{Zn}} = \frac{m_Y \times \rho_{Zn}}{m_{Zn} \times \rho_Y}$$

Substituting the atomic mass and densities of Yttrium and Zinc into the above equation we get the ratio of thickness required to be deposited,

$$\frac{t_Y}{t_{Zn}} = \frac{88.9 \times 7.13}{65.38 \times 4.49} = 2.164$$

That means Y must be sputtered at 2.164 times the rate (thickness deposited per unit time) at which Zn is being sputtered to get an equiatomic composition in the YZn films.

3.2 Calibration Methodology:

Calibration of the individual sputtering rates of Y and Zn is essential for achieving precise control over the composition of YZn thin films. The calibration methodology involves several steps, including the optimization of sputtering parameters, determination of the deposition rate, and monitoring of film thickness during deposition.

To optimize the sputtering parameters, the plasma power, pressure, and gas flow rate must be adjusted to obtain a stable plasma and a high deposition rate. The plasma power should be set to a level that produces a high-density plasma without causing target erosion. The pressure and gas flow rate should be controlled to maintain a uniform plasma and ensure a consistent deposition rate. The deposition rate of YZn thin films must be determined to achieve the desired thickness. This can be done by depositing a series of films with different deposition times and measuring the film thickness using techniques such as ellipsometry or profilometry, as has been previously discussed. The AJA Orion-5 magnetron sputtering system has an in-situ crystal thickness monitoring device based on quartz crystal microbalance technique. In-situ monitoring allows for real-time adjustments to the sputtering parameters to maintain a constant deposition rate and achieve the desired film thickness. The program controller helps to align the quartz thickness monitor to the appropriate material that is being sputtered, to determine the thickness precisely.

Initial calibration runs were performed separately for both the Y and Zn targets at varying powers while the Ar pressure was set at 3 mTorr and Ar flow at 14 sccm. It was found that at 55 W RF power, Zn targets had a deposition rate of 80 Å/min i.e., 8 nm/min. At this deposition rate, the required rate of Y can be found as 173.12 Å/min or 17.312

nm/min. Calibration runs for two of the Y targets were then performed and it recorded 170 Å/min deposition rate at 70 W and 194 Å/min deposition rate at 80 W. Interpolating these values for a 173.12 Å/min required rate and further conducting calibration runs, we end up with appropriate rate at 72 W power.

RUN	Y GUN 1 POWER	Y GUN 2 POWER	Zn POWER	PRESSURE	ARGON FLOW	DEPOSITION RATE	THICKNESS
1	72 W	72 W	55 W	3 mT	14 sccm	250 Å/min	115000 Å
2	72 W	72 W	55 W	3 mT	14 sccm	250 Å/min	20000 Å
3	72 W	72 W	55 W	3 mT	14 sccm	250 Å/min	10000 Å
4	72 W	72 W	55 W	3 mT	14 sccm	250 Å/min	5000 Å
5	72 W	72 W	55 W	3 mT	14 sccm	250 Å/min	2000 Å

Table 1: Summary of Sputtering Parameters for the YZn Films.

The calibration methodology described above ensures that the resulting YZn thin films are uniform and are of the correct composition and suitable for further annealing treatments and mechanical property measurements.

3.3 Film Deposition Methodology:

The deposition of YZn thin films involves a multi-step process that includes the preparation of the substrate, the loading of the sputtering targets, and the optimization of the sputtering parameters. The following section provides an overview of the deposition methodology for YZn thin films using the AJA Orion-5 magnetron sputtering system.

1. Substrate Preparation:

The substrate used for YZn thin film deposition is typically a Si wafer with a silicon oxide (SiO_2) layer on top. The SiO_2 layer is either a native oxide or a thermally grown oxide. Prior to deposition, the substrate must be cleaned to remove any contaminants that may interfere with the film's adhesion or purity. The cleaning process involves several steps, including solvent cleaning, followed by drying using compressed air.

2. Sputtering Target Loading:

Two Y targets and a single Zn target were used for depositing the YZn thin films. Two Y targets are required because the deposition rate for Y should be 2.16 times the sputtering rate of Zn to ensure an equiatomic composition of the YZn film. Moreover, the maximum DC power that can be applied to the Y targets cannot exceed 75 W because of the relatively low thermal conductivity of Y, which can lead to heating of the target during sputtering. On the other hand, Zn sputters easily and to accommodate the sputtering rate of Y, RF power, which leads to a lower sputtering rate, needs to be used on the Zn target.

3. Optimization of Sputtering Parameters:

The optimization of sputtering parameters is essential for achieving the desired film properties, such as thickness, composition, and morphology. The sputtering parameters that must be optimized include the plasma power, pressure, and gas flow rate. The plasma power is the amount of power applied to the sputtering target to generate a high-density plasma.

The pressure and gas flow rate are also critical parameters that must be optimized to achieve a uniform plasma and a consistent deposition rate. The pressure affects the density of the plasma, while the gas flow rate controls the amount of reactive gas introduced into the chamber during deposition. As has been discussed previously, the pressure, rate of flow and power has been set considering the required composition and deposition rate.

3.4 Characterization of YZn films:

The as-deposited YZn films were characterized by a variety of techniques including PXRD, SEM and Energy Dispersive X-ray Spectroscopy (EDS).

The PXRD scans (Fig. 7) showed that all the films, irrespective of the thickness, were amorphous in the as-deposited state. The scan data has been background subtracted and smoothed before plotting to enhance the clarity. The amorphous nature of the films can be inferred from the broad hump centered around 33 degrees that is present in all the films. Interestingly, the position of the amorphous peak is close to the (110) peak of the crystalline B2 YZn phase. As expected, the amorphous hump was more clearly visible in the thicker films because of the larger X-ray interaction volume which produces a stronger signal. For the thinnest films, the amorphous hump was barely visible. Importantly, none of the films showed any peaks corresponding to B2 YZn or other intermetallic compounds in the Y-Zn system. All the sharp peaks in the XRD scans can be traced back to the Si substrate.

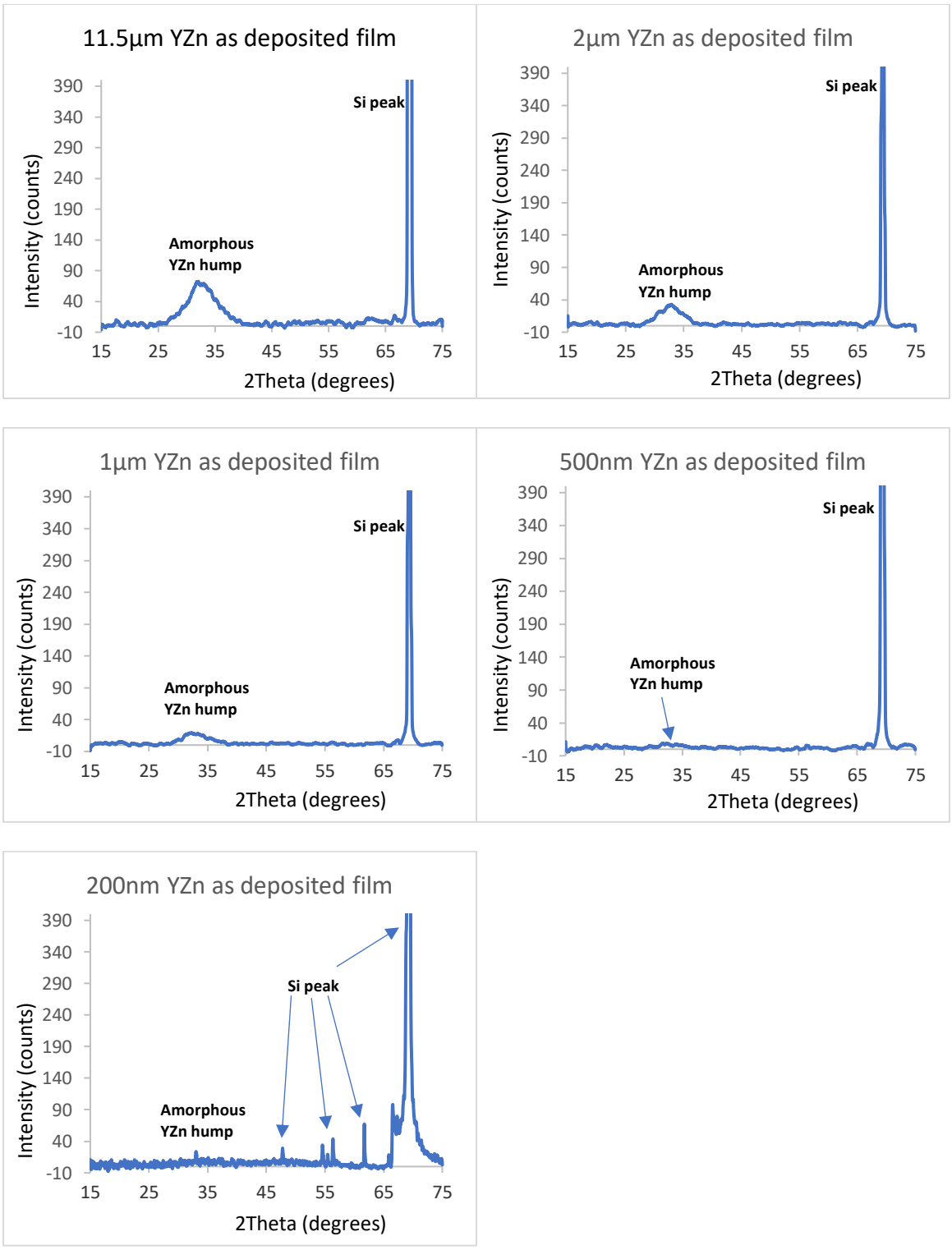

Figure 7: PXRD Results of As Deposited YZn Films of Various Thickness.

The surface of the as-deposited YZn films were characterized using SEM. The SEM images revealed an extremely smooth, featureless surface that is in marked contrast to polycrystalline films, which show clear features arising from grain boundary grooves. The absence of surface contrast in the SEM images reinforces the finding from PXRD that the as-deposited YZn films are amorphous.

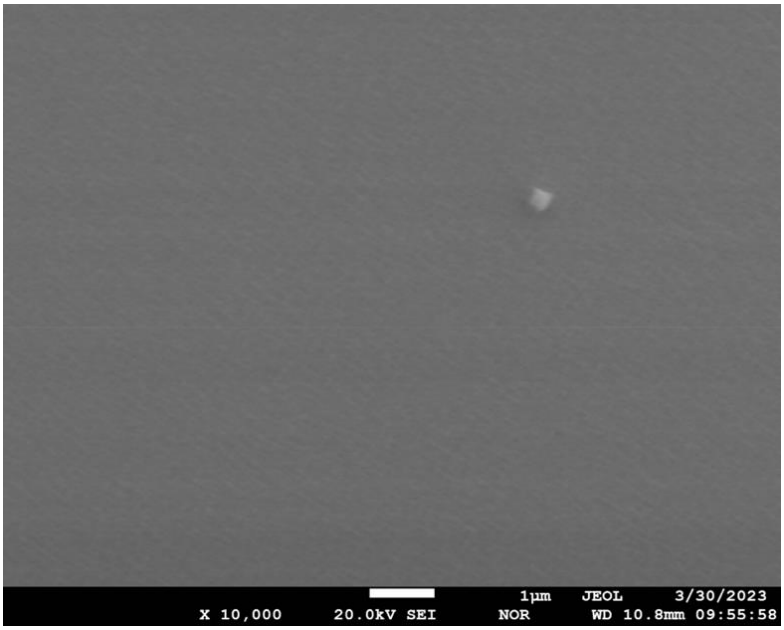

Figure 8: SEM Image of a 2µm Thick As-deposited YZn Film.

The compositional uniformity of the YZn films were assessed using Energy Dispersive X-ray Spectroscopy (EDS) in the SEM. EDS maps were obtained for the 2 µm and 11.5 µm thick from multiple locations, which showed that Y and Zn were uniformly distributed in the films without any preferential segregation.

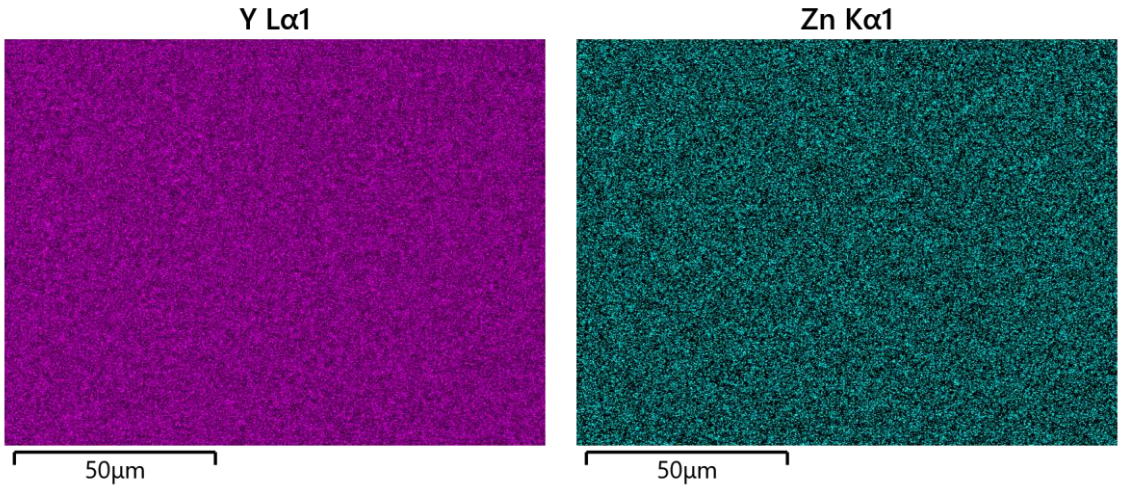

Figure 9: Y and Zn Distribution Map in the 2 µm Thick YZn Film.

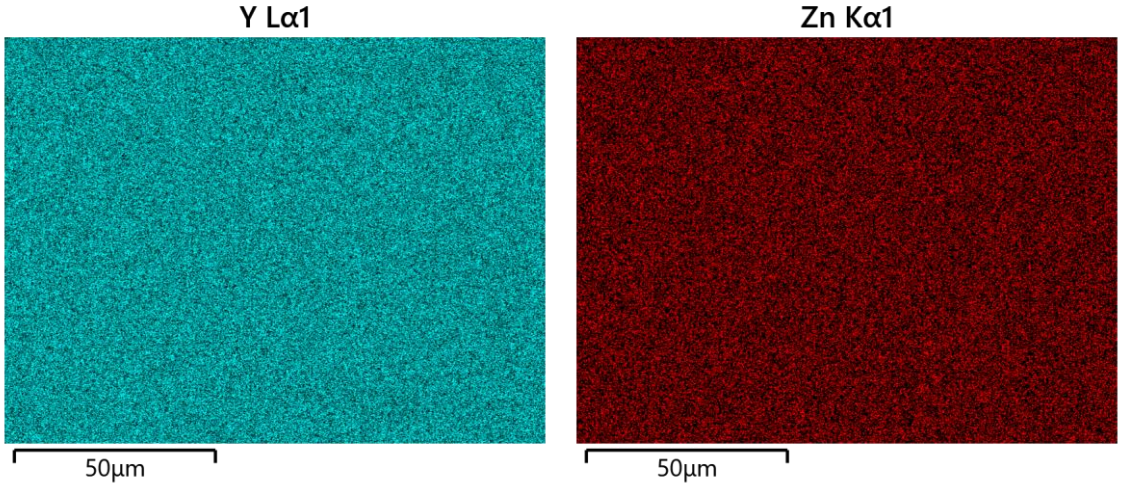

Figure 10: Y and Zn Distribution Map in the 11.5 µm Thick YZn Film.

3.5 Summary:

This chapter covered various topics related to the synthesis and characterization of YZn films. YZn films of 200 nm, 500 nm, 1 µm, 2 µm and 11.5 µm thickness were deposited by magnetron co-sputtering and characterized using PXRD, SEM and EDS. The XRD and SEM characterization revealed that all the YZn films were amorphous in the as-deposited state with a smooth, featureless surface. The EDS analysis showed a uniform distribution of Y and Zn within the films, with no evidence of segregation.

CHAPTER 4

ANNEALING EXPERIMENTS

4.1 Introduction

Annealing is a process in which a material is heated to a certain temperature and held for a certain period to induce changes in its structure, properties, and performance. Annealing studies are commonly conducted on thin films to investigate their structural evolution and stability at different temperatures. A controlled annealing process also allows for the optimization of film properties, such as crystallinity and grain size. In this chapter, we report on annealing studies conducted on YZn thin films of 5 different thicknesses, namely 11.5 µm, 2 µm, 1 µm, 500 nm, and 200 nm, each annealed at 4 different temperatures of 400°C, 350°C, 300°C, and 250°C.

4.2 Annealing Methodology & Discussions:

The YZn thin films of various thicknesses were co-deposited using AJA Orion 5 magnetron sputtering tool at room temperature, as previously detailed. The sputtering power of both Y and Zn was fixed, and the deposition time was adjusted to obtain the desired film thicknesses. One of the key capabilities of the AJA Orion 5 is its ability to anneal films at temperatures up to 850°C. The chamber can be evacuated to a base pressure lower than 5×10^{-8} Torr, which is necessary to maintain an oxygen free and stable environment for the annealing process. The high vacuum conditions also prevent contamination of the sample during annealing, which is important for achieving reproducible results. The samples were heated up to the desired temperatures of 400°C,

350°C, 300°C, and 250°C and then held at those temperatures for 4 hours before being cooled down to room temperature. The crystal structure of the YZn thin films was then analyzed using Powder X-ray diffraction (PXRD). The PXRD patterns were recorded with similar scan settings as that of the as-deposited samples described in Chapter 3.

For the 11.5 µm thick film, the as-deposited film was amorphous, and no crystalline phase was observed. After annealing, a B2 (110) peak of YZn was observed at higher annealing temperatures of 400°C and 350°C (Figure 11), with the highest intensity at 400°C. At lower annealing temperatures, almost no crystallinity was observed. The grain size remained relatively constant with increasing annealing temperature, with an average grain size of 6.6 nm at 350°C and 6.7 nm at 400°C (Table 2). The combined XRD plots for the as-deposited and annealed 11.5 µm thick film is shown in Figure 12.

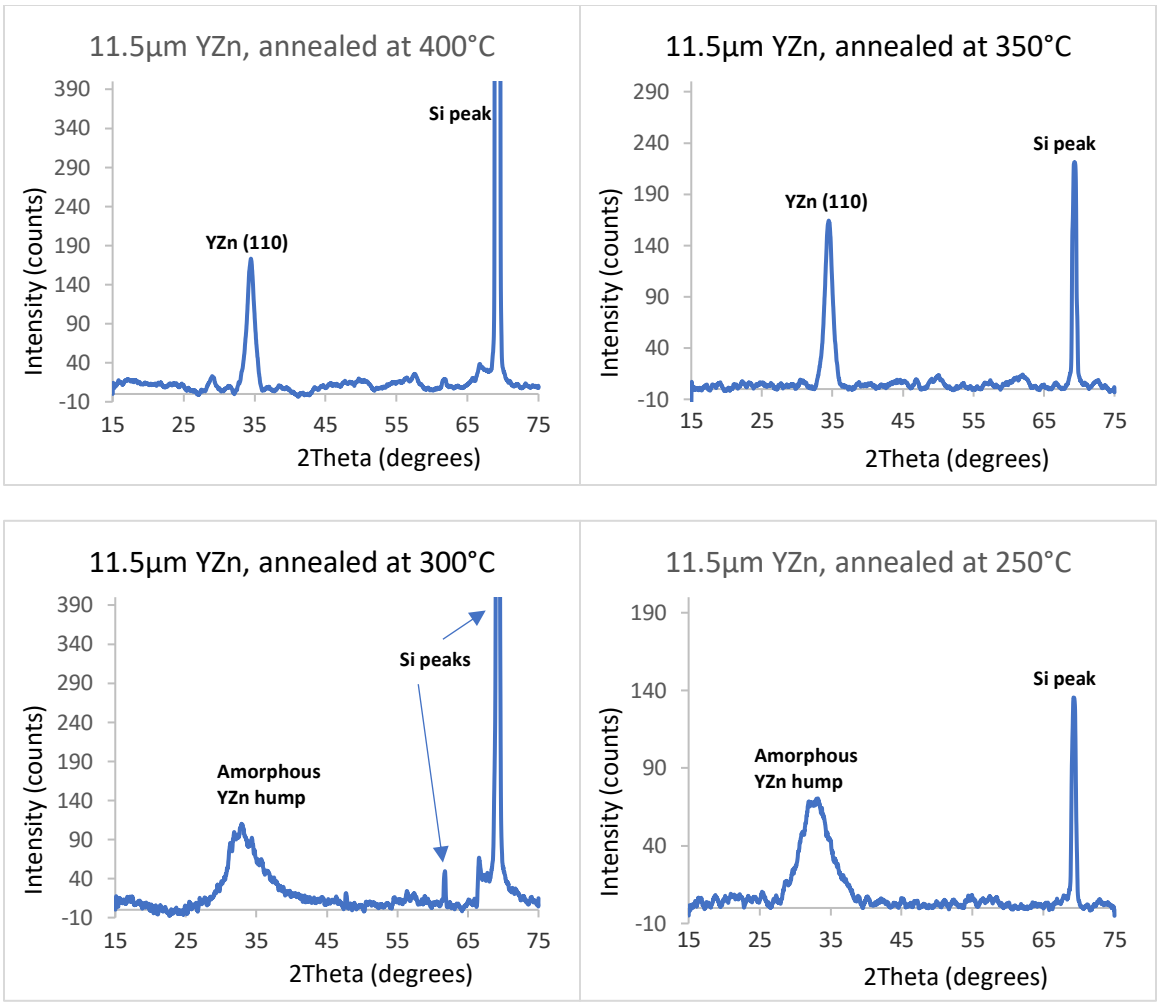

Figure 11: PXRD Results of 11.5 µm YZn Films Annealed at Different Temperatures.

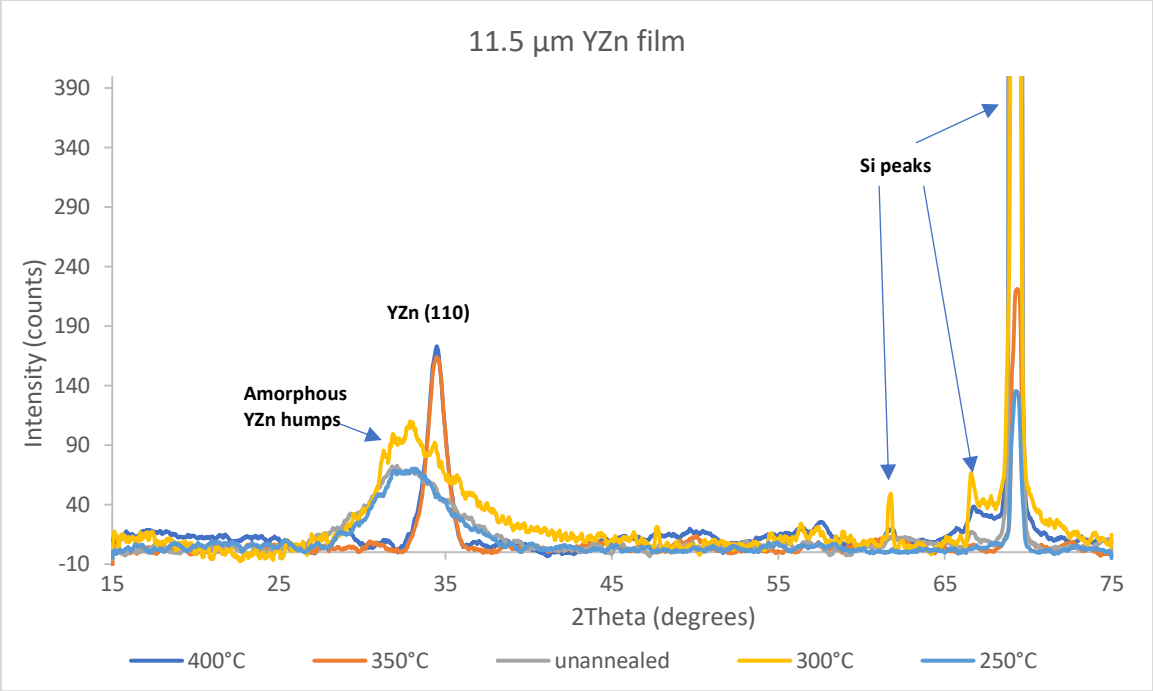

Figure 12: Comparison of PXRD Results of As-Deposited and Annealed, 11.5 µm YZn Films.

For the 2 μm thick films, the as-deposited film was also amorphous. After annealing at 400°C and 350°C, a (110) peak corresponding to the B2 phase of YZn was observed in the PXRD scan (Figure 13). However, there was another unidentified peak close to the (110) B2 peak, which suggests that the transformation to the B2 phase is not complete. The grain size slightly increased with increasing annealing temperature, from 4.4 nm at 350°C to 5.8 nm at 400°C (Table 2). At lower annealing temperatures, the film remained amorphous. The combined XRD plots for the as-deposited and annealed 2 μm thick film is shown in Figure 14.

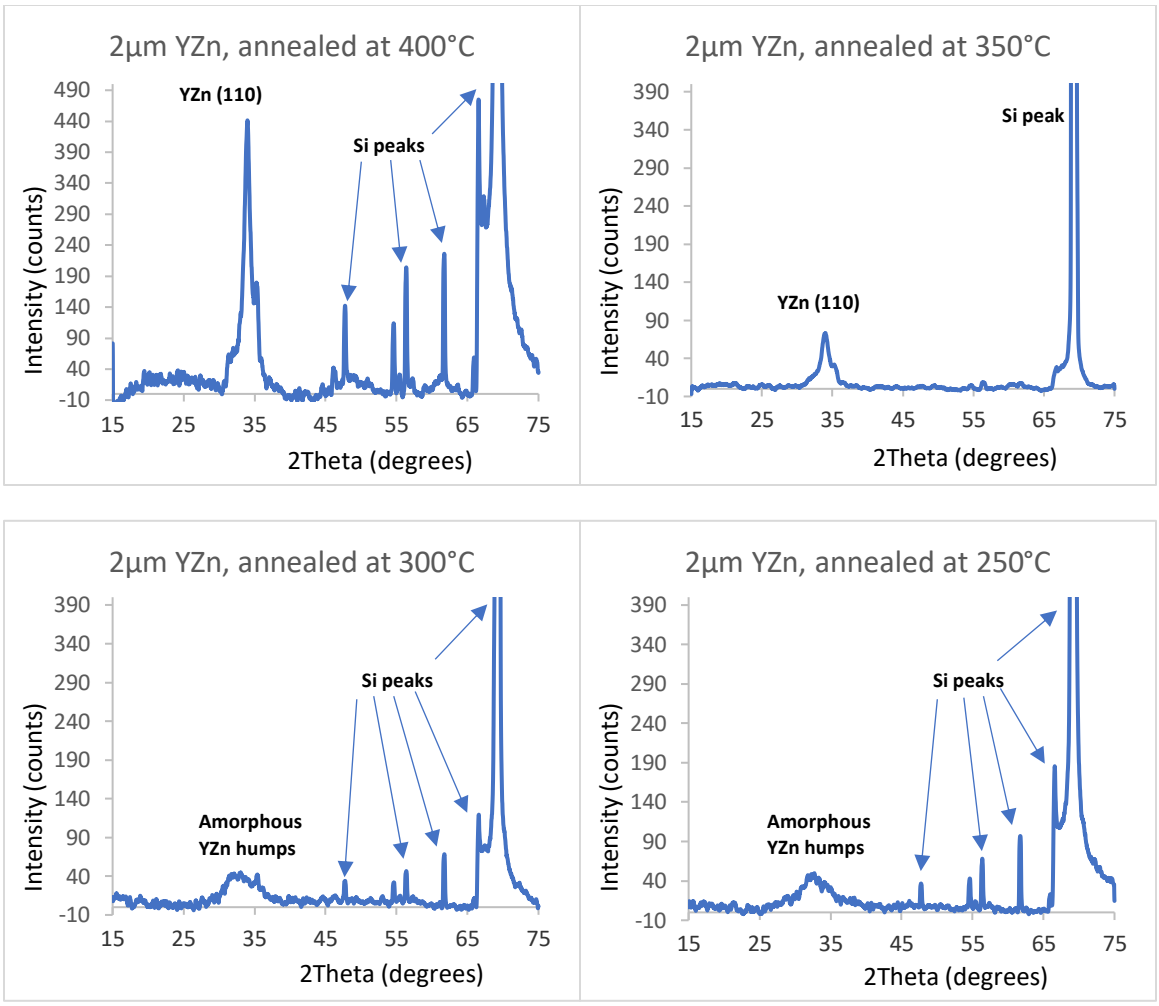

Figure 13: PXRD Results of 2 µm YZn Film Annealed at Different Temperatures.

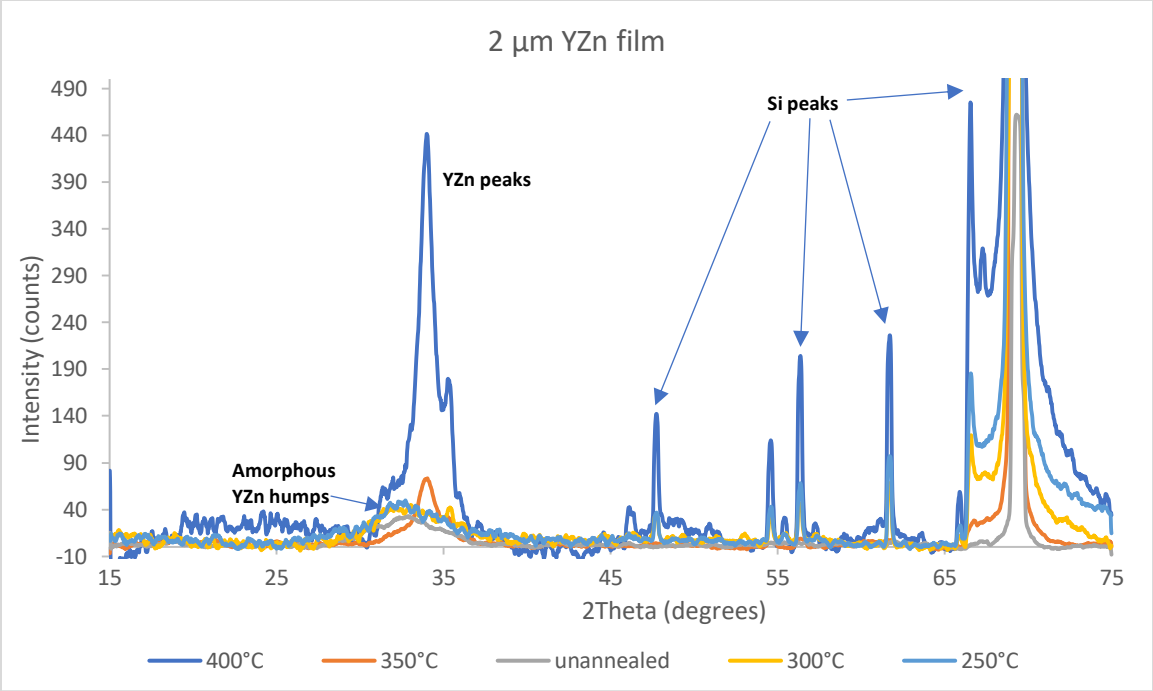

Figure 14: Comparison of PXRD Results of As-Deposited and Annealed 2 µm YZn Films.

For the 1 μm thick films, the as-deposited film was amorphous. The B2 phase of YZn was observed after annealing at 400°C and 350°C. However, an additional peak close to the (110) B2 peak was found in the 350°C annealed sample (Figure 15), which was also the case with the 2 μm thick film. The grain size decreased slightly with increasing annealing temperature, from 7.8 nm at 350°C to 6.8 nm at 400°C (Table 2). At lower annealing temperatures, the film remained amorphous. The combined XRD plots for the as-deposited and annealed 1 μm thick film is shown in Figure 16.

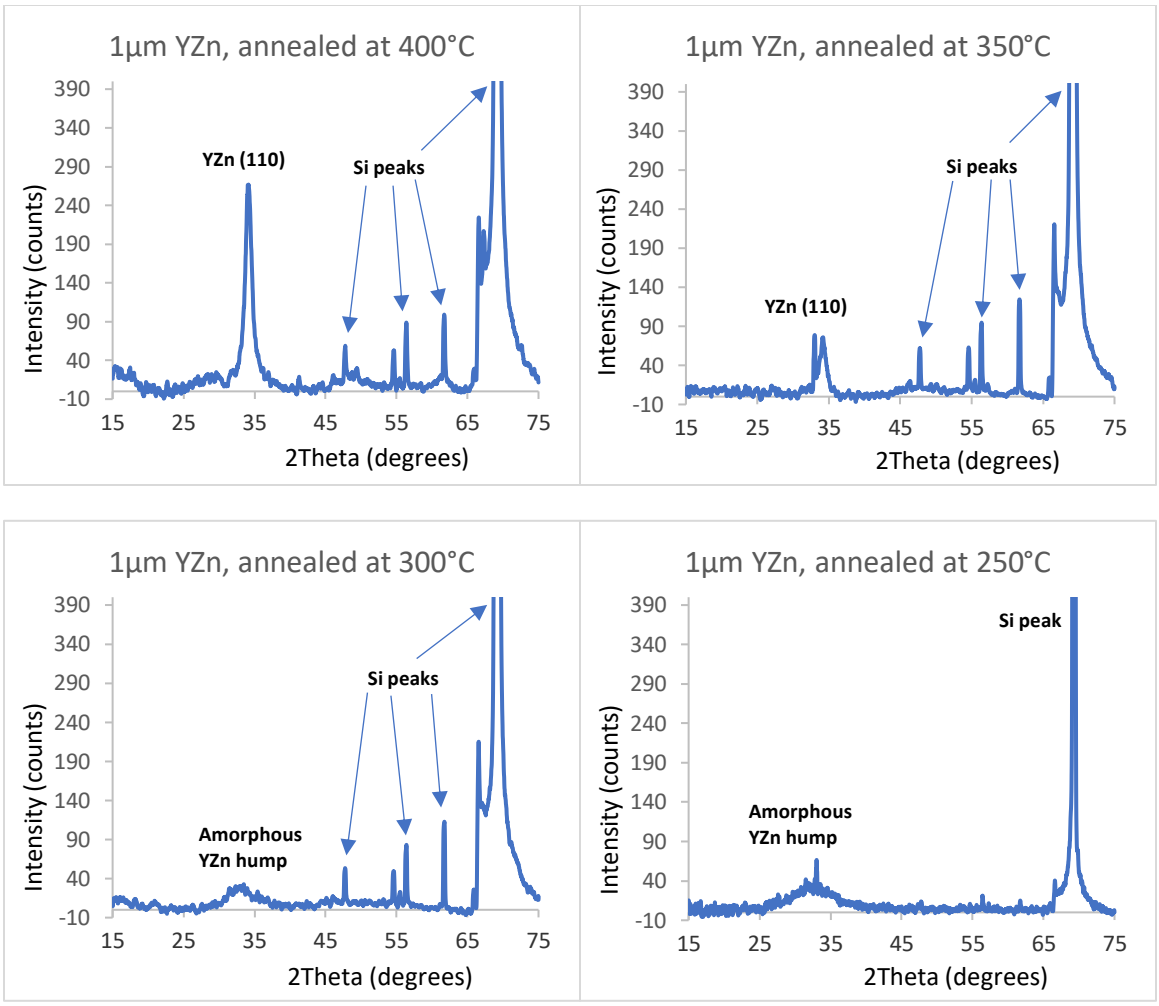

Figure 15: PXRD Results of 1 µm YZn Film Annealed at Different Temperatures.

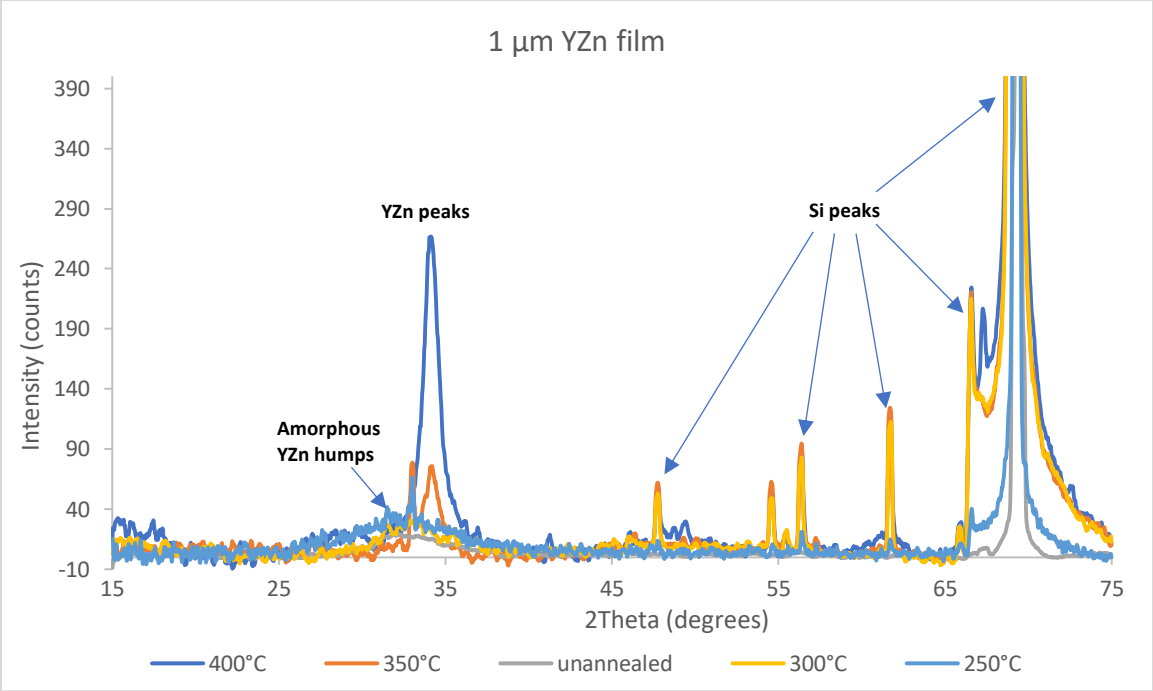

Figure 16: Comparison of PXRD Results of As-Deposited and Annealed 1 µm YZn Film.

For the 500 nm thick films, the as-deposited film was amorphous. The B2 phase of YZn was observed after annealing at 400°C and 350°C, as evidenced by the presence of the (110) peak (Figure 17), but the intensity of the peak was low compared to the thicker films. The mean grain size slightly increased with increasing annealing temperature, from 6 nm at 350°C to 7.2 nm at 400°C (Table 2). At lower annealing temperatures, the film remained amorphous. The combined XRD plots for the as-deposited and annealed 500 nm thick film is shown in Figure 18.

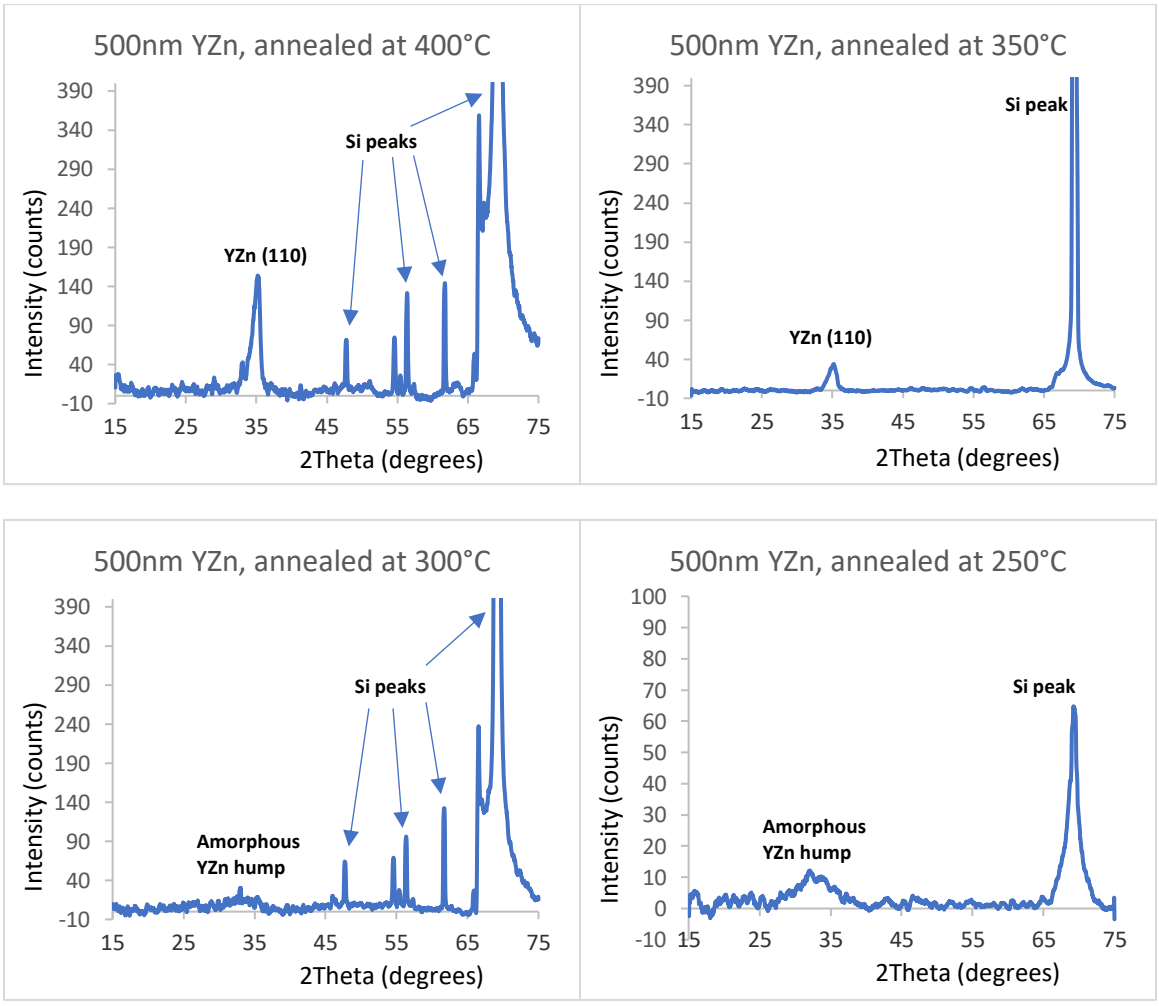

Figure 17: PXRD Results of 500 nm YZn Films Annealed at Different Temperatures.

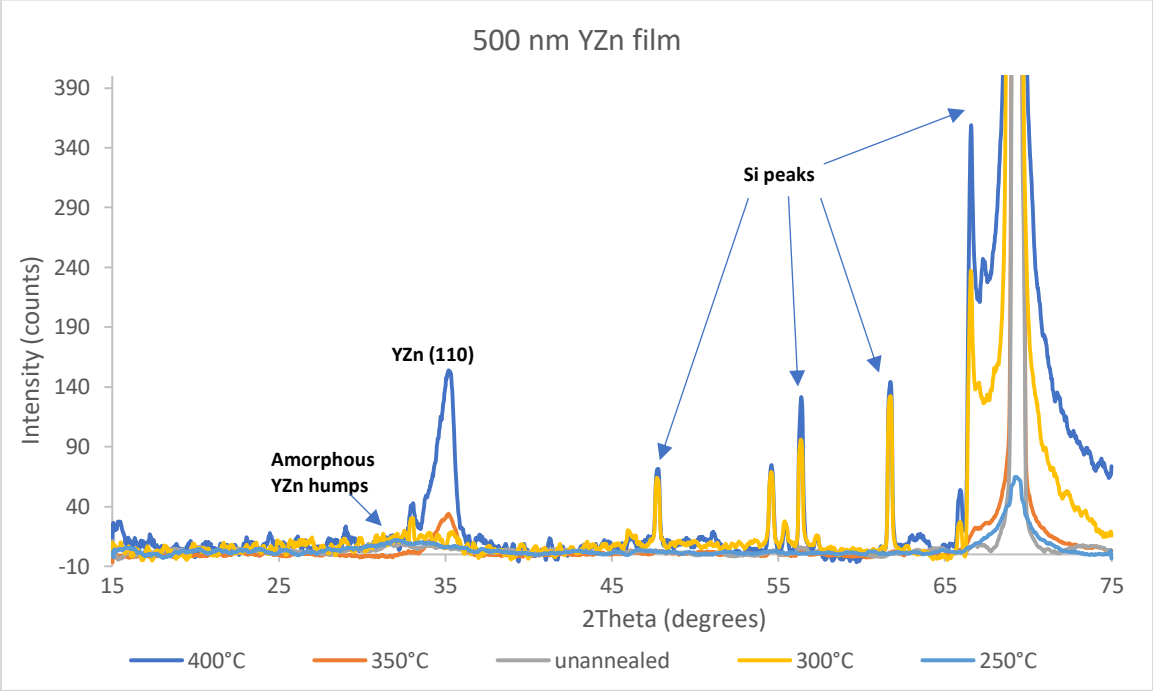

Figure 18: Comparison of PXRD Results of As-Deposited and Annealed 500 nm YZn Films.

For the thinnest YZn thin film (200 nm), the XRD patterns showed the formation of a B2 phase of YZn after annealing at 400°C and 350°C (Figure 19). Notably, the average grain sizes of the 200 nm film were considerably higher compared to the thicker films, with a value of 26.7 nm at 350°C annealing and 22.2 nm at 400°C annealing (Table 2). Interestingly, the samples annealed at 250°C and 300°C showed a peak around 33 degrees, which could correspond to the (220) peak of YZn_2. The combined XRD plots for the as-deposited and annealed 200 nm thick film is shown in Figure 20.

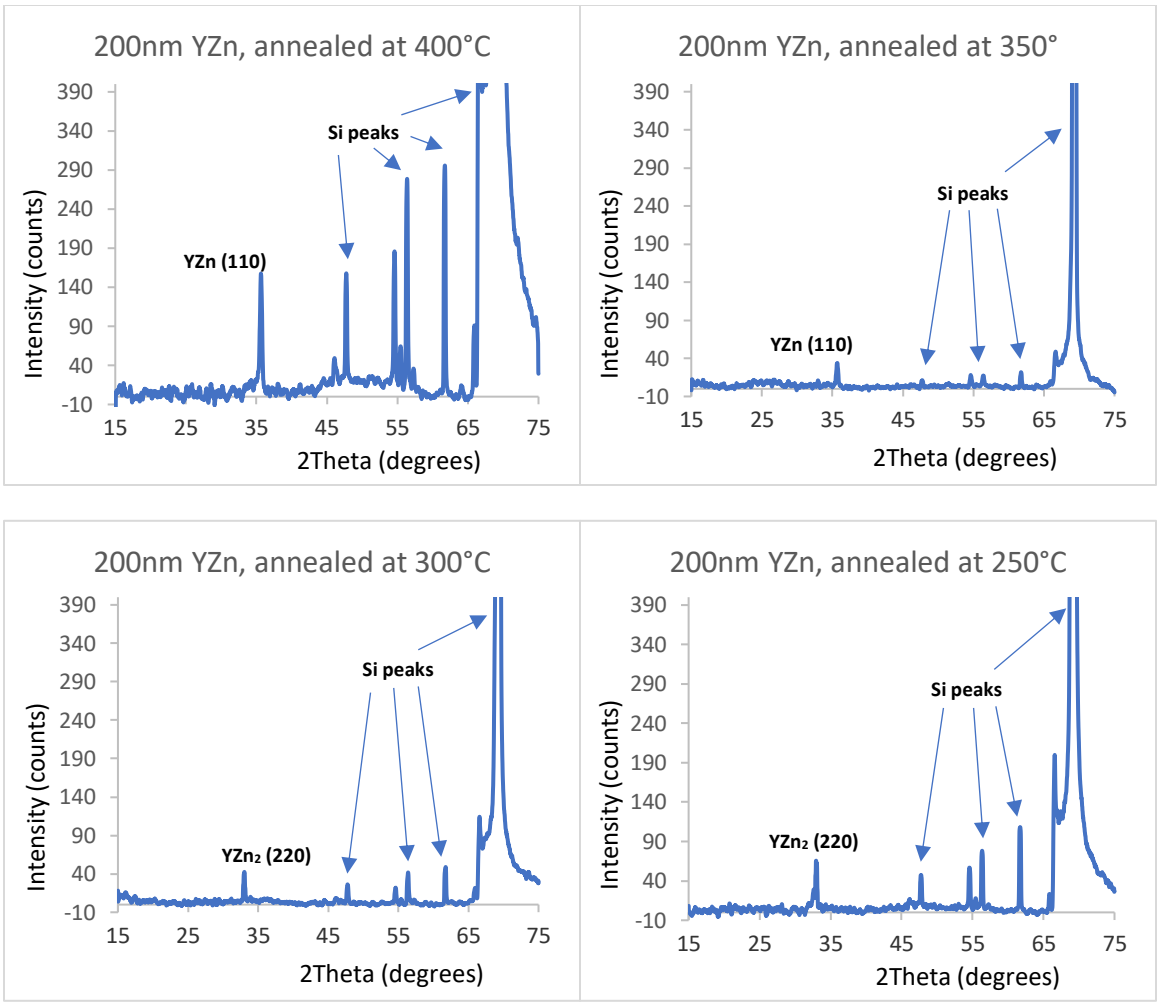

Figure 19: PXRD Results of 200 nm YZn Films Annealed at Different Temperatures.

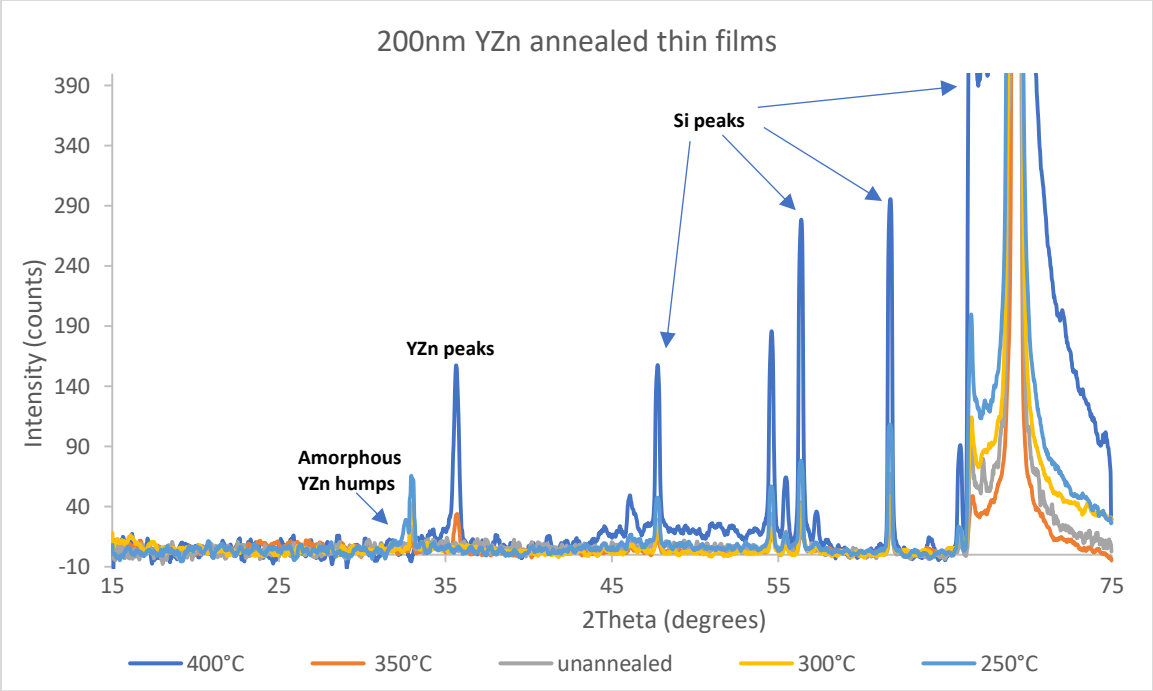

Figure 20: Comparison of PXRD Results of As-Deposited and Annealed 200 nm YZn Films.

Thickness (μm)	350 °C Annealed sample			400 °C Annealed sample		
	β (rad.)	2θ (deg.)	D (Å)	β (rad.)	2θ (deg.)	D (Å)
11.5	0.022895	34.48149	66.22795	0.02251	34.46085	67.36062
2	0.03442	33.97006	43.9899	0.02625	33.9585	57.6791
1	0.01931	34.1756	78.4626	0.02241	34.1531	67.59676
0.5	0.02501	35.00047	60.70524	0.02103	35.1529	72.2178
0.2	0.00571	35.68342	266.4883	0.00685	35.65198	222.1208

Table 2: Estimated Grain Size Calculations of YZn Films after Annealing at 350°C & 400°C.

4.3 Summary:

In summary, the annealing studies conducted on YZn thin films of 5 different thicknesses showed that all films exhibited the B2 phase of YZn after annealing at 400°C and 350°C, with the highest intensity observed for the 11.5 μm thick film (Figure 21). Apart from the (110) B2 peak, additional peaks were found in some of the films at various temperatures which suggests that intermediate phases may be nucleated before the formation of the thermodynamically stable B2 phase in these YZn films. The grain size of the crystallized YZn films did not show notable changes with thickness. This is in stark contrast to metallic films that are crystalline in the as-deposited state, where the grain size typically scales with the thickness. The thickness independence of the grain size in the YZn films can be explained by the fact the grain nucleation occurs primarily from defects (excess free volume) within the amorphous film. Since the density of the defects should be independent of the film thickness, the average distance between the nucleation sites should be the same for all films and hence their final grain size is also roughly similar. The one exception to this trend is the 200 nm film, which has the lowest thickness. The larger grain size in this film can be attributed to the dominance of surface nucleation over nucleation in the bulk.

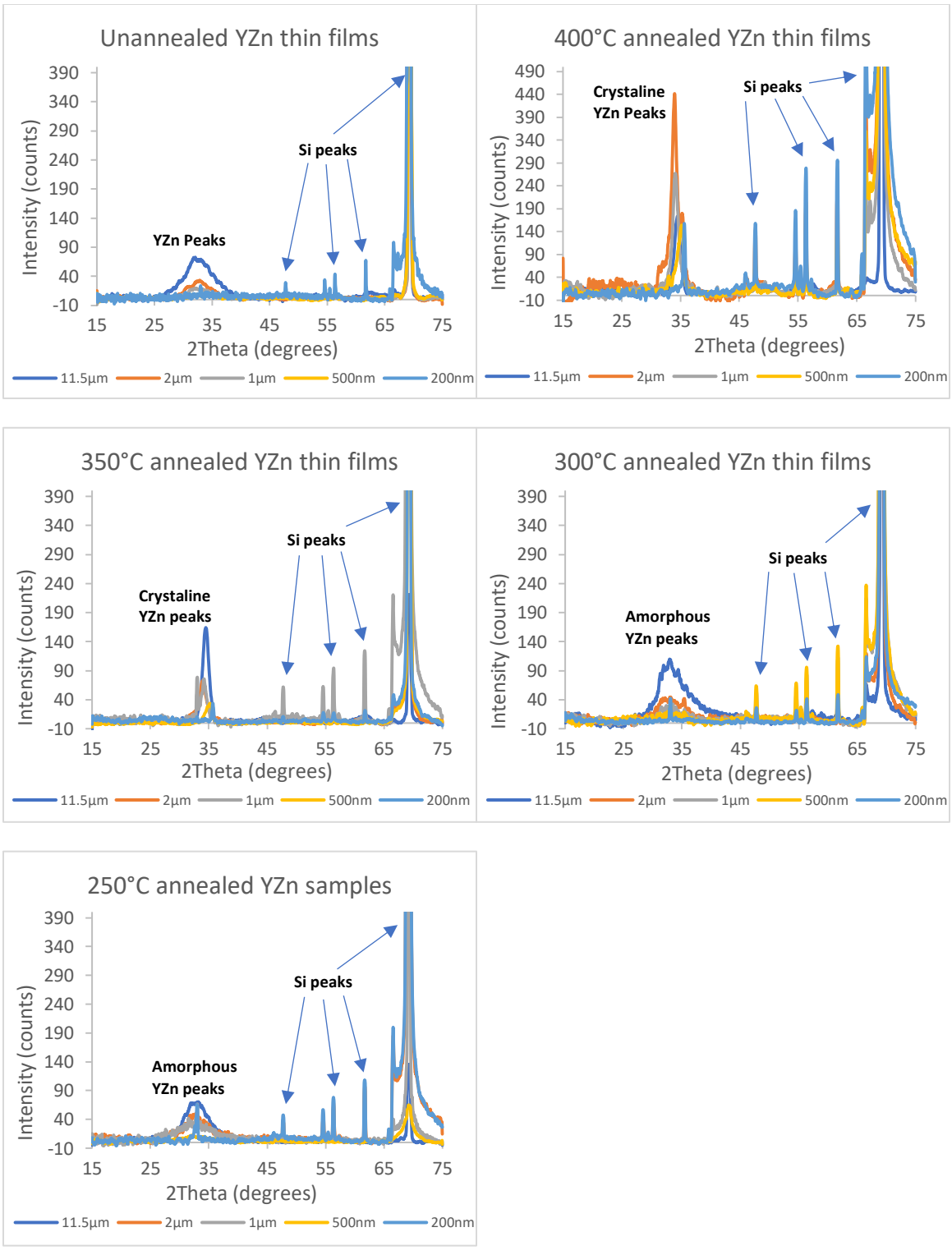

Figure 21: Comparison of PXRD Results of Annealed YZn Films at Each Temperature.

CHAPTER 5

NANOINDENTATION STUDIES ON YZn FILMS

5.1 Introduction:

We examined the mechanical properties of the YZn films through nanoindentation to discern the trends in Young's modulus (E) and hardness (H) as a function of annealing temperature and thickness. For this study, we used only the 11.5 μm and 2 μm thick films since an indentation depth of around 150 nm is required to get consistent values of E and H, and the film thickness needs to be at least 10 times that of the indentation depth to avoid substrate effects. The Hysitron TI 980 triboindenter was used for the nanoindentation study and the indentations were performed in the displacement-controlled mode. More details of the nanoindentation methodology can be found in the paper, Radiation tolerance and microstructural changes of nanocrystalline Cu-Ta alloy to high dose self-ion irradiation by Srinivasan etal., 2020.[28]

We selected the as-deposited sample and the samples annealed at 250°C and 400°C of the 11.5 μm and 2 μm thick films for nanoindentation. This was done because the as-deposited samples are amorphous whereas the 400°C annealed samples are crystalline, and one should expect a significant change in E and H upon crystallization. The 250°C annealed samples are also amorphous but are expected to have structural changes compared to the as-deposited sample, which might also lead to changes in E and H.[29] A minimum of 9 indentations were performed on each sample at locations separated by at least 25 μm to obtain reliable statistics on E and H. Representative load-displacement curves obtained from nanoindentation of each of the six samples is shown in Figure 22.

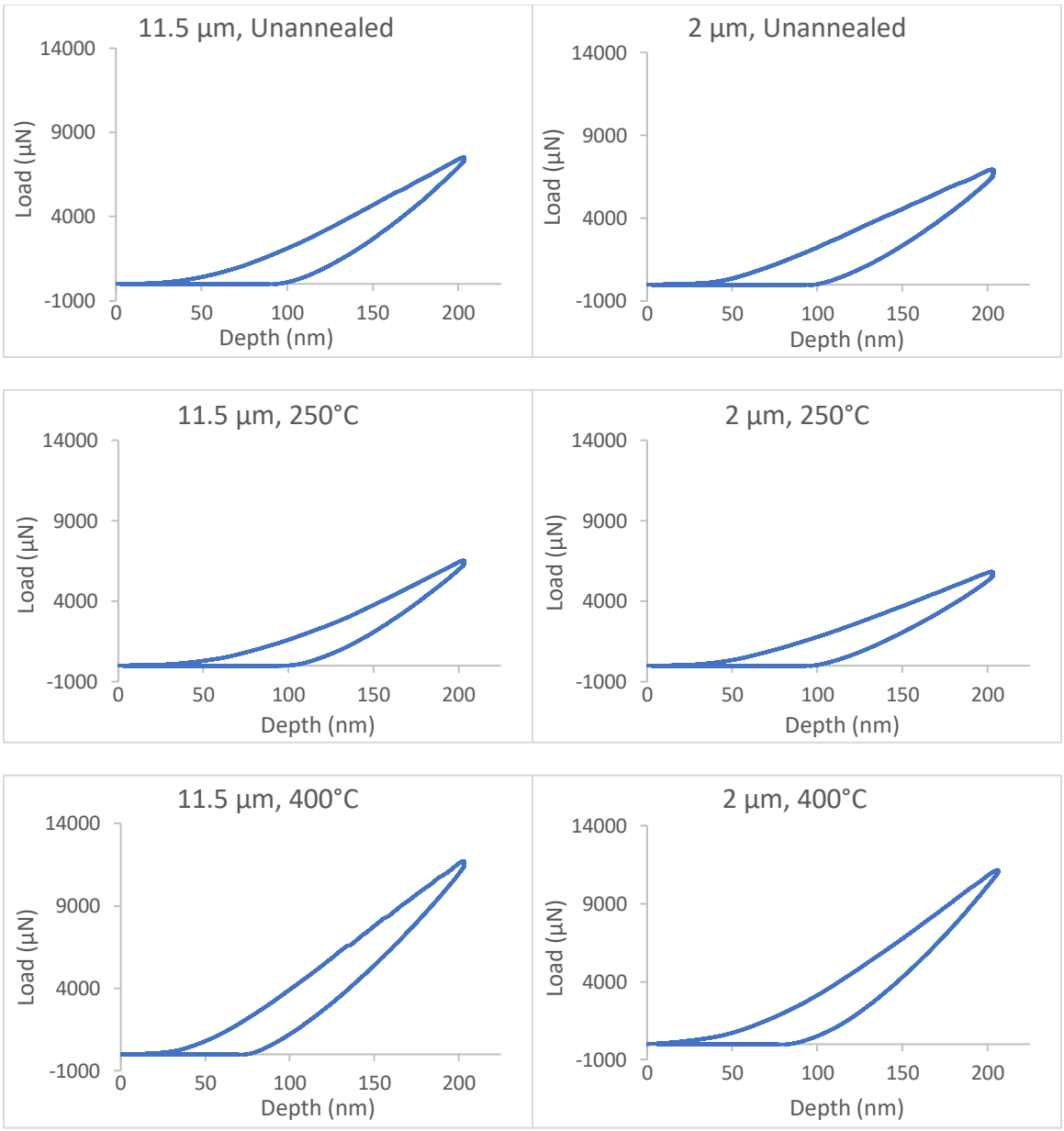

Figure 22: Load Vs Displacement Graph for the Samples from Nanoindentation Experiments.

5.2 Mechanical properties of 11.5 μm YZn film:

The plots of E and H for the 11.5 μm YZn film in the as deposited, 250°C annealed and 400°C annealed conditions are shown in Figure 23. As evident from Figure 23, both E and H are highest for the 400°C annealed sample. The higher E of 400°C annealed sample is expected because the sample is fully crystalline, and the Young's modulus of crystalline intermetallic films are typically higher than their amorphous counterparts.[30] The higher H of the 400°C annealed sample is somewhat unexpected because amorphous intermetallic films are usually harder than their polycrystalline counterparts. However, this result can be explained by the extremely fine grain size of the 400°C annealed sample, which would result in a substantial increase in H because of the Hall-Petch effect.

Surprisingly, both E and H for the 250°C annealed sample are lower than that of the as deposited sample. Usually, annealing metallic glass films below the crystallization temperature results in an increase in both H and E due to structural relaxation.[31] However, in this case we see the opposite trend. While the exact reason for this observation is unclear, one possibility is that intermediate phases that have a lower E and H could form at 250°C before the B2 YZn phase is nucleated at higher temperatures.

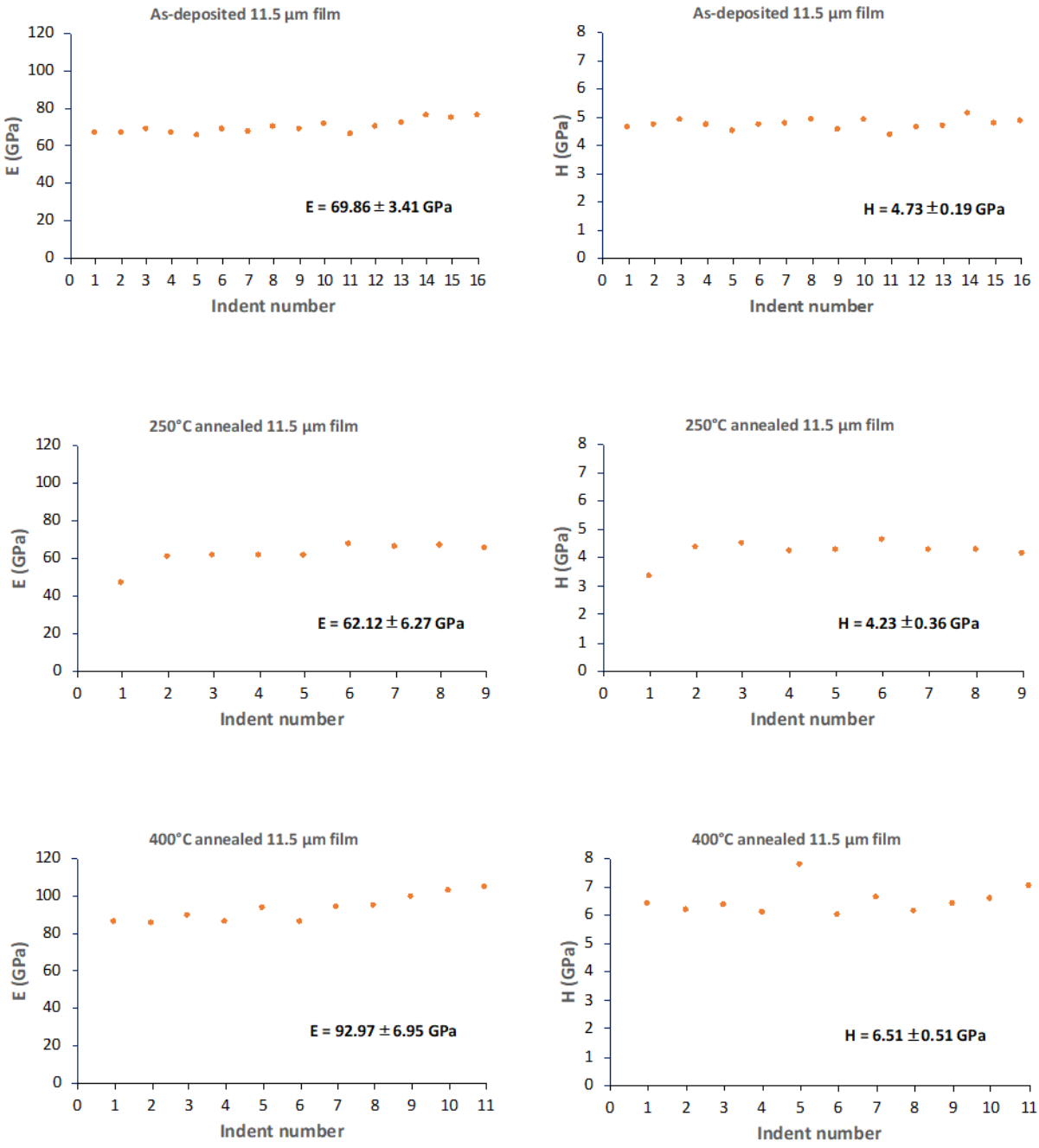

Figure 23: Young's Modulus and Hardness of 11.5µm Film in the as Deposited and Annealed Conditions.

5.3 Mechanical properties of 2 μm YZn film:

The plots of E and H for the 2 μm YZn film in the as deposited, 250°C annealed and 400°C annealed conditions are shown in Figure 24. As evident from Figure 24, for the 2 μm film both E and H are highest for the 400°C annealed sample. The same result was seen in the 11.5 μm film and can be attributed to the crystalline nature of the 400°C annealed sample. Similarly, the higher H of the 400°C annealed 2 μm film can also be explained by the extremely fine grain size of the sample (Hall-Petch effect).

As with the case of the 11.5 μm film, both E and H for the 250°C annealed sample are lower than that of the as deposited sample, which could be due the formation of an intermediate phase with a lower E and H compared to the B2 phase. Although there are some unresolved questions, the nanoindentation results of the 11.5 μm film and 2 μm film show broadly consistent trends with the thicker film exhibiting consistently higher E and H for all annealing conditions.

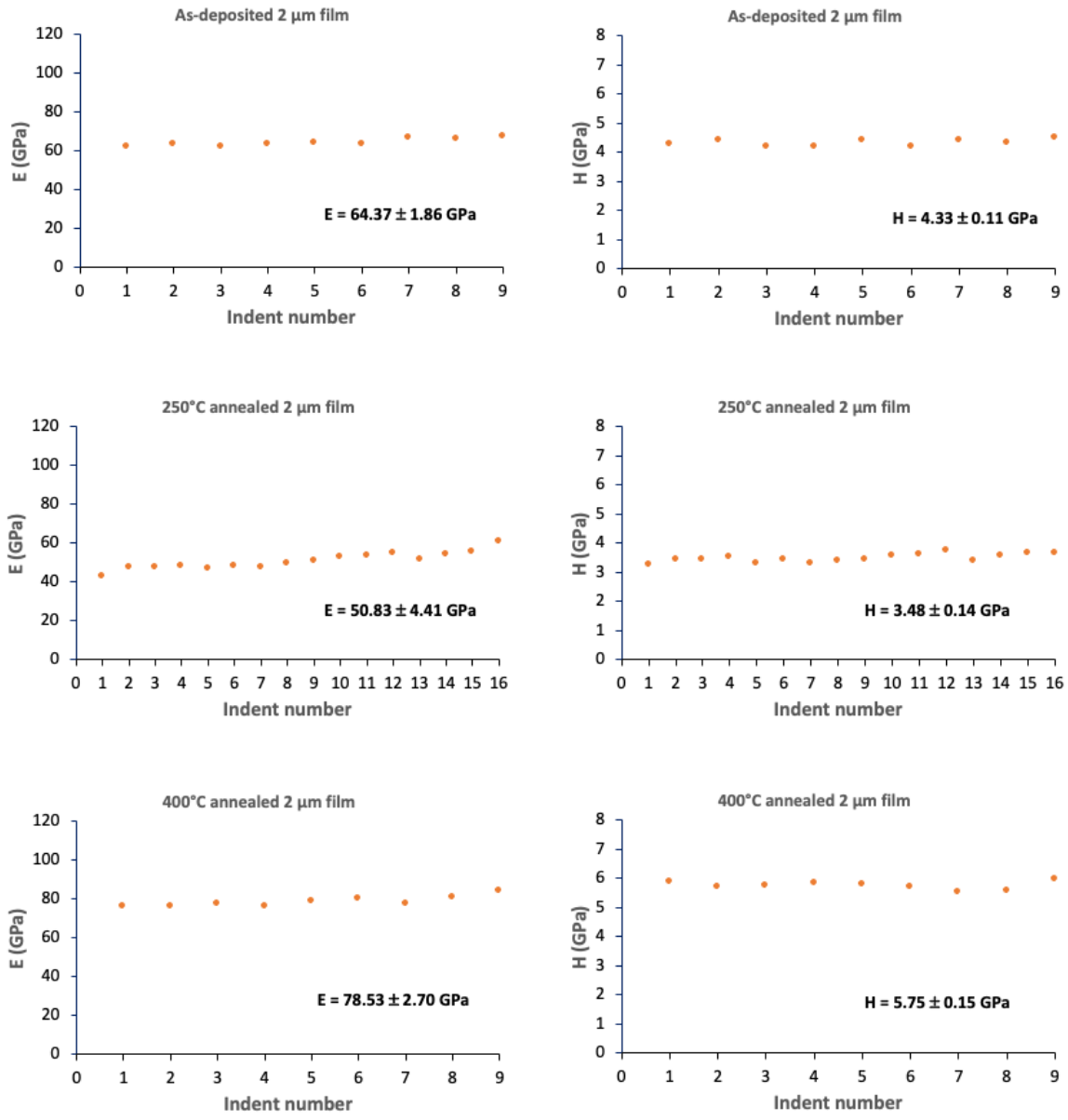

Figure 24: Young's Modulus and Hardness of 2 µm Film in the as Deposited and Annealed Conditions.

CHAPTER 6

CONCLUSION

6.1 Summary of research findings:

The synthesis of YZn films of various thicknesses - 11.5 µm, 2 µm, 1 µm, 500 nm, and 200 nm - was successfully achieved using magnetron sputtering. The individual sputtering rates of Y and Zn were calibrated as a function of sputtering power. Based on this calibration, appropriate powers were chosen for the Y and Zn targets to achieve an equiatomic composition.

The YZn films were found to be amorphous in the as-deposited state by X-ray diffraction analysis. The surface of the as-deposited YZn films were characterized using SEM, which revealed an extremely smooth, featureless surface. EDS analysis of the films showed that Y and Zn were uniformly distributed in the films without any preferential segregation.

Annealing studies were conducted over temperatures of 400 °C, 350 °C, 300 °C, and 250 °C for 4 hours each. The results showed that higher annealing temperatures (400 °C and 350 °C) led to crystallization, whereas lower temperature annealing did not except for the 200 nm film. In all cases, crystallization led to the formation of the B2 phase.

The mechanical properties of the 11.5 µm and 2 µm thick films were examined in the as-deposited (amorphous), 250°C annealed (amorphous) and 400°C annealed (crystalline) states using nanoindentation. The nanoindentation study revealed that the crystallized sample had the highest hardness and Young's modulus for both the 11.5 µm

and 2 µm thick film. However, the hardness and Young's modulus of the 250°C annealed sample was lower than the as-deposited sample for both films.

6.2 Future scope:

This study has demonstrated the synthesis of YZn films of various thicknesses using magnetron sputtering. Although the as-deposited films are amorphous, annealing of the films at sufficiently high temperatures leads to crystallization and an increase in Young's modulus and hardness. Interestingly, annealing at temperatures lower than the crystallization temperature results in a reduction of Young's modulus and hardness. Further studies are required to understand this unusual reduction in Young's modulus and hardness. DSC studies can be conducted to determine whether any intermediate phases, which result in the reduction of mechanical properties, evolve before the nucleation of the thermodynamically stable B2 phase. Tensile testing of the YZn films can be performed using MEMS devices to measure the yield strength, ductility, and toughness as function of film thickness and annealing treatment.[32]

With regard to microstructural evolution, in-situ TEM studies can reveal the mechanism of crystal nucleation in the YZn films and point to potential routes to control the grain size. Furthermore, since the as-deposited YZn films are amorphous, it is possible to use seed layers to control the crystallization process and obtain specific microstructures and mechanical properties.[33][34]

REFERENCES

[1] Roman Gumeniuk, Chapter 304 - Structural and Physical Properties of Remeika Phases, Handbook on the Physics and Chemistry of Rare Earths, Elsevier, Volume 54, 2018, Pages 43-143, ISSN 0168-1273, ISBN 9780444641595, https://doi.org/10.1016/bs.hpcre.2018.10.001.

[2] J.W. Fergus, 1.25 - High Temperature Corrosion of Intermetallic Alloys, Shreir's Corrosion, Elsevier, 2010, Pages 646-667, ISBN 9780444527875, https://doi.org/10.1016/B978-044452787-5.00078-0

[3] The Cambridge Crystallographic Data Centre, https://www.ccdc.cam.ac.uk/elements/yttrium/, Accessed: 3/30/2023.

[4] B.S. Murty, J.W. Yeh, S. Ranganathan, Chapter 7 - Intermetallics, Interstitial Compounds and Metallic Glasses in High-Entropy Alloys, High Entropy Alloys, Butterworth-Heinemann, 2014, Pages 119-131, ISBN 9780128002513, https://doi.org/10.1016/B978-0-12-800251-3.00007-9

[5] Materials explorer, The Materials Project, https://materialsproject.org/materials/mp-2516?chemsys=Y-Zn, Accessed: 3/30/2023.

[6] Mason, J.T., Chiotti, P. Phase diagram and thermodynamic properties of the yttrium-zinc system. Metall Mater Trans A 7, 289 (1976), https://doi.org/10.1007/BF02644469.

[7] Jantao Tan, Jun Wang, Qing Cao, Hailin Bi, Jun Wu, Xudi Wang, High-rate deposition of ultra-thick silver film by hollow cathode magnetron sputtering, Vacuum, Volume 212, 2023, 112034, ISSN 0042-207X, https://doi.org/10.1016/j.vacuum.2023.112034.

[8] Zhou Lu, Xin Lv, Quan Xie, Magnetron-sputtered gallium–magnesium–zinc oxide transparent semiconductor thin films: Structural, optical and electrical investigation, Optik, Volume 265, 2022, 169301, ISSN 0030-4026, https://doi.org/10.1016/j.ijleo.2022.169301.

[9] Kholida Tul Khairy, Yeongha Song, Jang-Hee Yoon, José Montero, Lars Österlund, Seohan Kim, Pungkeun Song, Thermochromic properties of vanadium oxide thin films prepared by reactive magnetron sputtering at different oxygen concentrations, Vacuum, Volume 210, 2023, 111887, ISSN 0042-207X, https://doi.org/10.1016/j.vacuum.2023.111887.

[10] Milton Ohring, Chapter 5 - Plasma and Ion Beam Processing of Thin Films, Editor(s): Milton Ohring, Materials Science of Thin Films (Second Edition), Academic Press, 2002, Pages 203-275, ISBN 9780125249751, https://doi.org/10.1016/B978-012524975-1/50008-2.

[11] AJA International Inc.,
https://www.ajaint.com/atc-orion-series-sputtering-systems.html, Accessed: 3/30/2023.

[12] AJA International Inc. AJA Orion-5 Magnetron Sputtering System [Photograph]. Retrieved from https://www.ajaint.com/uploads/2/9/6/4/29644999/1421185906.png, Accessed: 3/30/2023.

[13] Oliver, W. C., & Pharr, G. M. (2004). Measurement of hardness and elastic modulus by instrumented indentation: Advances in understanding and refinements to methodology. Journal of Materials Research, 19(1), 3-20.

[14] Bhushan, B. (2009). Principles and applications of tribology. John Wiley & Sons.

[15] Ronald F. Gibson, A review of recent research on nanoindentation of polymer composites and their constituents, Composites Science and Technology, Volume 105, 2014, Pages 51-65, ISSN 0266-3538, https://doi.org/10.1016/j.compscitech.2014.09.016.

[16] Albrecht, HJ., Hannach, T., Häse, A. et al. Nanoindentation: a suitable tool to determine local mechanical properties in microelectronic packages and materials?. Arch Appl Mech 74, 728–738 (2005). https://doi.org/10.1007/s00419-005-0394-5.

[17] C.E. Carlton, P.J. Ferreira, In situ TEM nanoindentation of nanoparticles, Micron, Volume 43, Issue 11, 2012, Pages 1134-1139, ISSN 0968-4328, https://doi.org/10.1016/j.micron.2012.03.002.

[18] Donna M. Ebenstein, Lisa A. Pruitt, Nanoindentation of biological materials, Nano Today, Volume 1, Issue 3, 2006, Pages 26-33, ISSN 1748-0132, https://doi.org/10.1016/S1748-0132(06)70077-9.

[19] Han, Chung-Souk & Sanei, Seyed Hamid Reza & Alisafaei, Farid. (2015). On the origin of indentation size effect and depth dependent mechanical properties of elastic polymers. Journal of Polymer Engineering. 10.1515/polyeng-2015-0030.

[20] Tsui, T.Y., Pharr, G.M. Substrate effects on nanoindentation mechanical property measurement of soft films on hard substrates. Journal of Materials Research 14, 292–301 (1999). https://doi.org/10.1557/JMR.1999.0042.

[21] VanLandingham, M.R., Villarrubia, J.S., Guthrie, W.F. and Meyers, G.F. (2001), Nanoindentation of polymers: an overview. Macromol. Symp., 167: 15-44. https://doi.org/10.1002/1521-3900(200103)167:1<15::AID-MASY15>3.0.CO;2-T.

[22] Reeta Asmai, UC Davis. PANalytical Xpert Pro XRD Machine [Photograph]. Retrieved from https://mse.engineering.ucdavis.edu/amcat/panalytical-xpert-pro-mrd, Accessed: 3/30/2023.

[23] Scherrer, P. (1918). Bestimmung der Grösse und der inneren Struktur von Kolloidteilchen mittels Röntgenstrahlen [Determination of the size and internal structure of colloidal particles using X-rays]. Nachr. Ges. Wiss. Göttingen, Math-Phys. Klasse, 2, 98-100, http://eudml.org/doc/59018.

[24] Van Berkum, J. G. M., Vermeulen, A. C., Delhez, R., de Keijser, T. H., & Mittemeijer, E. J. (1994). Applicabilities of the Warren–Averbach analysis and an alternative analysis for separation of size and strain broadening. Journal of applied crystallography, 27(3), 345-357.

[25] Muralt, P., Polcawich, R., & Trolier-McKinstry, S. (2009). Piezoelectric Thin Films for Sensors, Actuators, and Energy Harvesting. MRS Bulletin, 34(9), 658-664. doi:10.1557/mrs2009.177, https://doi.org/10.1557/mrs2009.177

[26] R. Berlia, J. Rajagopalan, Synthesis of Heterostructured Metallic Films with Precisely Defined Multimodal Microstructures, ACS Appl. Mater. Interfaces. 13 (2021) 46097–46104. https://doi.org/10.1021/acsami.1c10999.

[27] R. Berlia, P. Rasmussen, S. Yang, J. Rajagopalan, Tensile behavior and inelastic strain recovery of Cu-Co nanolaminates, Scripta Materialia. 197 (2021) 113781. https://doi.org/10.1016/j.scriptamat.2021.113781.

[28] Srinivasan, S., Kale, C., Hornbuckle, B. C., Darling, K. A., Chancey, M. R., Hernández-Rivera, E., ... & Solanki, K. N. (2020). Radiation tolerance and microstructural changes of nanocrystalline Cu-Ta alloy to high dose self-ion irradiation. Acta Materialia, 195, 621-630.

[29] Gu, J., Song, M., Ni, S., Guo, S., & He, Y. (2013). Effects of annealing on the hardness and elastic modulus of a Cu36Zr48Al8Ag8 bulk metallic glass. Materials & Design, 47, 706-710.

[30] R. Sarkar, C. Ebner, E. Izadi, C. Rentenberger, J. Rajagopalan, Revealing anelasticity and structural rearrangements in nanoscale metallic glass films using in situ TEM diffraction, Materials Research Letters. 5 (2017) 135–143. https://doi.org/10.1080/21663831.2016.1228709.

[31] Chen, C. S., Yiu, P., Li, C. L., Chu, J. P., Shek, C. H., & Hsueh, C. H. (2014). Effects of annealing on mechanical behavior of Zr–Ti–Ni thin film metallic glasses. Materials Science and Engineering: A, 608, 258-264.

[32] R. Berlia, J. Rajagopalan, Mechanical behavior of heterostructured iron films with precisely defined bimodal architectures, Acta Materialia. 237 (2022) 118193. https://doi.org/10.1016/j.actamat.2022.118193.

[33] R. Sarkar, J. Rajagopalan, Synthesis of thin films with highly tailored microstructures, Materials Research Letters. 6 (2018) 398–405. https://doi.org/10.1080/21663831.2018.1471420.

[34] P. Rasmussen, R. Berlia, R. Sarkar, J. Rajagopalan, Mechanical behavior of nanocrystalline and ultrafine-grained NiTi thin films, Materialia. 15 (2021) 100994. https://doi.org/10.1016/j.mtla.2020.100994.